Justus-Liebig-Universität Gießen
I. Physikalisches Institut

Electrical Transport Properties of Doped Gallium Nitride Nanowires

D i s s e r t a t i o n

zur Erlangung des Doktorgrades
der Naturwissenschaften
Doctor rerum naturalium
(Dr. rer. nat.)

vorgelegt dem

Fachbereich 07
Mathematik und Informatik, Physik, Geographie

von

Diplom-Physiker

Markus Georg Schäfer

Gießen, im November 2014

Betreuung:
Prof. Dr. Martin Eickhoff
AG Nanotechnologische Materialien

In der Mitte von Schwierigkeiten liegen die Möglichkeiten.

Albert Einstein

Contents

Zusammenfassung

Gegenstand dieser Arbeit ist die Untersuchung elektrischer Transporteigenschaften einzelner dotierter Gruppe III-Nitrid Nanodrähte. Zum ersten Mal wird der Einfluss von Germanium als flacher Donator in Galliumnitrid Nanodrähten, die mittels Molekularstrahlepitaxie gewachsen wurden, untersucht.
Das Wachstum der Galliumnitrid Nanodrähte auf Silizium(111) Substraten wurde in einer Molekularstrahlepitaxie Anlage durchgeführt und basiert auf einem selbstassemblierten Prozess ohne Katalysator. Abhängig von Dotierung und Wachstumszeit haben die Nanodrähte einen Durchmesser zwischen 30 nm und 120 nm sowie eine Länge von 1 µm bis 2 µm.
Zur elektrischen Charakterisierung einzelner Nanodrähte wurde ein Prozess zur Mikro- und Nanostrukturierung, basierend auf einer Kombination aus Foto- und Elektronenstrahllithographie, entwickelt, um individuell gestaltete, wenige Nanometer breite und präzise platzierte metallische Kontakte zu realisieren. Einzelne Nanodrähte konnten schließlich in vielfältigen Geometrien kontaktiert werden, um dem jeweiligen Anspruch der Messung gerecht zu werden. Beispielsweise konnten Nanodrähte mit nur 1 µm Länge mit vier und 2 µm lange Drähte sogar mit sechs individuellen Kontakten versehen werden. Dabei konnte eine sehr hohe Überdeckungsgenauigkeit mit einer Abweichung zwischen Layout und Ergebnis von weniger als 10 nm realisiert werden.
Einzelne kontaktierte Nanodrähte wurden auf verschiedene Weisen untersucht. Durch Vierleitermessungen, die den Einfluss der Kontaktwiderstände ausschließen, konnte bei bekannter Geometrie der Nanodrähte die elektrische Leitfähigkeit bestimmt werden. Die Geometrie des untersuchten Stücks des Nanodrahts wurde durch Analyse mittels Rasterelektronenmikroskopie bestimmt. Durch Vergleich mit Zweipunktmessungen konnte darüber hinaus die Größe des Kontaktwiderstands ermittelt werden. Für nominell undotierte Nanodrähte wurden sowohl hoch resistive als auch leitfähige Drähte identifiziert. Für letztere wurde eine erhöhte Leitfähigkeit an der Basis des Drahtes festgestellt, was auf eine Diffusion von Silizium aus dem für das Wachstum verwendeten Siliziumsubstrat in die Nanodrähte zurückgeführt wurde. Für Nanodrähte dotiert mit Germanium konnte ein kontinuierlicher Anstieg der Leitfähigkeit mit steigender Germaniumkonzentration beobachtet werden. Temperaturabhängige Messungen zeigten

eine schwache Aktivierung und konstante Leitfähigkeit für tiefe Temperaturen. Für einen Nanodraht wurde sogar metallisches Verhalten beobachtet. Eine Analyse der temperaturabhängigen thermoelektrischen Eigenschaften der Nanodrähte ermöglichte die Bestimmung der Konzentration freier Ladungsträger. Es wurden Ladungsträgerdichten von bis zu $5.5 \times 10^{19}\,\mathrm{cm}^{-3}$ deutlich über dem Metall-Isolator-Übergang für Galliumnitrid (etwa $2 \times 10^{18}\,\mathrm{cm}^{-3}$) nachgewiesen. Photolumineszenz-Spektroskopie an einzelnen Nanodrähten zeigte eine schwache Zunahme der Breite der Emission, wohingegen keine spektrale Verschiebung mit steigender Ladungsträgerkonzentration beobachtet wurde. Durch die Kombination der Ergebnisse von Leitfähigkeitsmessungen und Ladungsträgerdichtebestimmung konnte die Beweglichkeit der Ladungsträger abgeschätzt werden. Silizium-dotierte Nanodrähte wurden zum Vergleich untersucht. Dabei konnte kein signifikanter Einfluss, des während dem Wachstums zusätzlich angebotenen Silizium auf die elektrische Leitfähigkeit, im Vergleich zu nominell undotierten Nanodrähten, nachgewiesen werden.
Die verschiedenen Messungen stehen in Einklang miteinander und zeigen systematisch, dass Germanium ein effektiver flacher Donator in Galliumnitrid Nanodrähten ist.

Abstract

In this thesis a systematic characterization of the electrical transport properties of single gallium nitride nanowires is presented. For the first time germanium as a shallow donor in gallium nitride nanowires grown by plasma-assisted molecular beam epitaxy is analyzed.

To access electrical measurements on a single nanowire level a process technology to contact nanowires with a length of 1 µm was developed and established. The process benefits from fast parallel patterning by photolithography and individual designed nanosized structures by electron beam lithography. After optimization of all process parameters an alignment mismatch smaller than 10 nm is achieved and single nanowires can be contacted in different layouts to address the needs of individual measurements. Comparative electrical transport measurements in four-point and two-point geometry revealed a significant influence of the contact resistance. Two different types of non-intentionally doped wires were observed: highly resistive and conductive nanowires. The origin of the conductivity was investigated by spatially resolved conductivity measurements and is partially attributed to diffusion of silicon from the substrate into the non-intentionally doped nanowires. The conductivity of germanium-doped nanowires increases continuously with increasing concentration of germanium. The influence of the nanowire diameter on the conductivity was investigated as well. The carrier concentration was determined by temperature-dependent analysis of the Seebeck coefficient. Carrier concentrations above the metal insulator transition were revealed. The almost temperature-independent conductivity can be assigned to the formation of an impurity band and even metallic behavior, indicated by a positive temperature coefficient of the resistivity, was found. The near band edge emission analyzed by micro-photoluminescence spectroscopy showed only a small increase of the peak width and no spectral shift with increasing carrier concentration. The latter is attributed to the simultaneous influence of band filling, band gap renormalization, and strain. For the investigated Si-doped NWs no significant influence of increasing Si supply during growth on the conductivity, in comparison to non-intentionally doped NWs, was observed.

Chapter 1

Motivation

Today's modern life is dominated by electronic devices. Personal computers, smartphones and a variety of other instruments influence our private lives. But even if the private consumer sector is excluded, a life without electronic devices is hardly imaginable. ATMs, cars, medical devices, or even the supply chain of food in supermarkets would not be operated without electronics. The present information age is often called „silicon age“ in the media. This naming is of course referenced to the currently dominant complementary metal-oxide-semiconductor (CMOS) technology based on silicon (Si), but various other modern achievements of material research are acknowledged as well. As an example, gallium arsenide based high-frequency electronics or gallium nitride based light emitting diodes are mentioned.

Driven by Moore's Law, the semiconductor industry has been working by all means to achieve continuous down-scaling of devices. Moore noted that the complexity of minimum cost semiconductor components had doubled per year since the first prototype microchip was produced in 1959. This exponential increase in the number of components on a chip is known as Moore's Law. Its interpretation changed during the following years [1]. In the 1980s, Moore's Law started describing the doubling of number of transistors on a chip every 18 months. At the beginning of the 1990s, Moore's Law became commonly interpreted as the doubling of microprocessor power every 18 months. Later it became widely associated with the claim that computing power at fixed cost is doubling every 18 months. In any case, the end of Moore's Law was seen close at hand several times, but technical sophistication and new ideas have opened doors for further development and progress. The International Technology Roadmap for Semiconductors (ITRS) sets the standards for continued progress in this industry for years. Due to the fact that further down-scaling, called „More Moore“, lead to immense costs and financial risk and certainly will reach the ultimate limit set by the laws of thermodynamics some day, a second strategy was developed. Referring to Moore's law the strategy is called „More than Moore“ [2]. It means that instead of

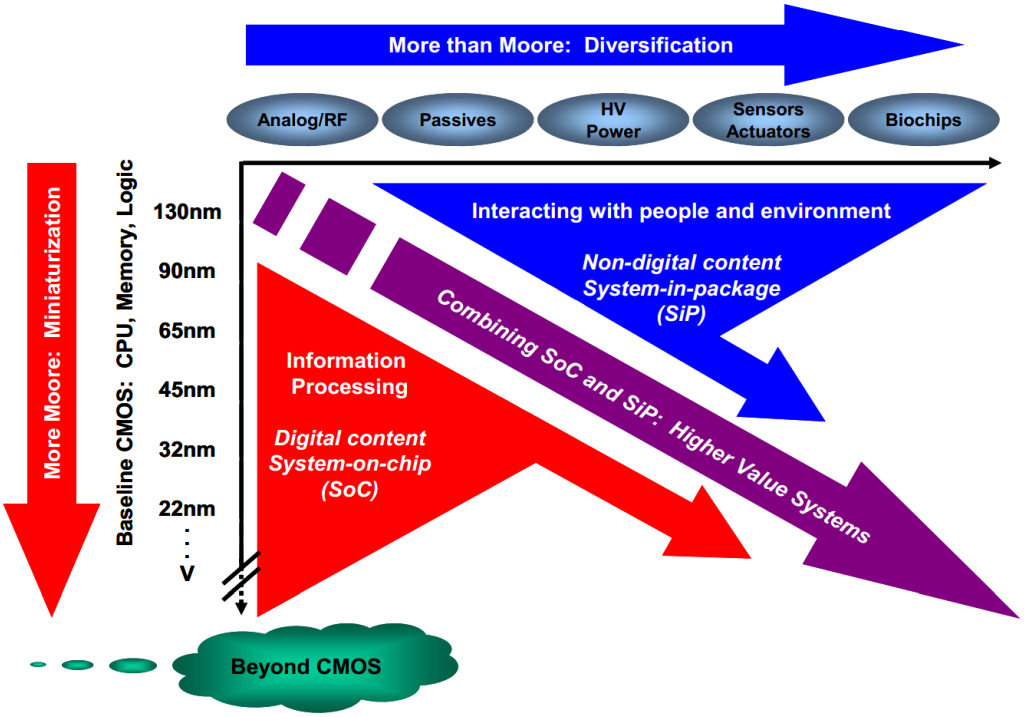

Figure 1.1.: The combined need for digital and non-digital functionality in an integrated system is translated as a dual trend in the International Technology Roadmap for Semiconductors. NWs has the potential to be a key technology for both miniaturization called „More Moore“ and diversification named „More than Moore“. Figure taken from ref. [2]

smaller structures more features and non-digital functionality should be migrated from the system board-level into the package (SiP) or onto the chip (SoC) as depicted in **Figure 1.1**. The terms SiP and SoC or lab-on-a-chip describe the combination of sensors and actuators or optoelectronic components with logic electronics in one unit. Less power consumption and lower cost compared to the conventional combination is the advantage.

In particular, NWs could be a key technology to serve both strategies. Instead of sophisticated, very expensive and complex top-down-approaches the bottom-up growth of NWs could lead to advantageous nano-sized structures to fulfill Moore's law in the „More Moore“ sense. In addition, NWs have been proven to be excellent sensors for a variety of applications and open up an enormous field for lab-on-a-chip applications in the sense of „More than Moore“ [3]. On-chip combination of silicon-based logic and group III-V NW based optoelectronics could be a solution for future optical computation. A sticking point for the success of hybrid systems is the reliability and scalability of NW integration processes.

NWs are officially included in the ITRS since more than 10 years as a solution for

the technology of the day after tomorrow, the „beyond CMOS“ age. The ITRS of 2013 says in the section „Emerging Research Devices (ERD)“: „*III-V nanowires offer the potential advantages of higher mobility, on-off current ratio, and subthreshold swing than can be achieved with conventional silicon circuitry. The ease with which the band structure can be engineered also opens the possibility for transistors that use two-dimensional electron gas conduction for even higher mobility than can be achieved in the homojunctions, or for devices based on tunneling through epitaxial barrier layers made from semiconductor layers with higher band gap*“[1], but still a long way of research and development is ahead. Scientists and companies all over the world study the potential and feasibility of nanowires made of various materials.
The European Union had funded the project „NANOFUNCTION“[2] from 2010 to 2013 with EUR 3 million to explore nano-devices for adding functionality to CMOS. Within the „HORIZON 2020“ framework the European Commission proposes a new European strategic industrial research and innovation program „Innovation for the future of Europe: Nano-electronics beyond 2020“ with a total investment of EUR 100 billion up to 2020. The project „Electronic Components and Systems for European Leadership“ (ECSEL) will start 2014 and is funded with EUR 5 billion for ten years.[3]
Today just the tip of the iceberg of NW based technology is discovered. As a fundamental requirement for any kind of application using NWs precise knowledge and control of doping is needed. Therefore, to add a small piece to the puzzle of future NW electronics, the investigation of the influence of doping on the electrical properties of gallium nitride nanowires is the focus of research in this thesis.

[1] http://www.itrs.net/Links/2013ITRS/2013Chapters/2013ERM.pdf
[2] FP7-ICT, 257375, http://cordis.europa.eu/result/brief/rcn/11809_de.html
[3] http://europa.eu/rapid/press-release_MEMO-13-673_en.htm

Chapter 2

Introduction

Group III-nitrides have been considered as a promising material base for semiconductor device applications since 1970. The group III-nitrides, with the binary compounds aluminum nitride (AlN), gallium nitride (GaN), and indium nitride (InN) are excellent candidates for optoelectronic applications such as blue-, UV- and IR-light emitting diodes, because they form a continuous alloy system (InGaN, InAlN, and AlGaN) whose direct optical bandgap for the hexagonal wurtzite phase ranges from 0.7 eV for InN over 3.4 eV for GaN to 6.2 eV for AlN [4, 5] as depicted in **Figure 2.1**. The wide band gap with large breakdown electric fields makes the material suitable for high power applications as well. Heterostructures with a discontinuity in total polarization are used to build high electron mobility transistors (HEMT) based on a 2-dimensional electron gas [4, 6].

Due to the fact that GaN substrates suited for homo-epitaxy are small and very expensive GaN thin films are most often grown by hetero-epitaxy on substrates as sapphire, Si(111), and SiC. The large lattice mismatch leads to a high density of defects, lowering the achievable device performance.

Due to lattice mismatch compensation by strain relaxation at lateral surfaces in the region closed to the interface to the substrate [8] nanowires exhibit excellent crystalline and optical quality being superior to thin films. Suitable reported substrates beside silicon(111), that is used for the growth of the NWs investigated in this thesis [9, 10], are diamond [11] and sapphire [12]. Consequently, wide and direct band gap GaN NWs attracted a lot of research and commercial interest for nanoscaled (opto)-electronic devices [13]. Big effort is expended in solid state lighting [14] and photovoltaics based on group-III-nitride NWs as well.

In addition to the outstanding structural and optical properties, the high surface to volume ratio of NWs make them suitable for applications as chemical sensors [15, 16, 17, 18, 19, 20, 21, 22, 23], photo detectors [24] and field effect transistors [25, 26].

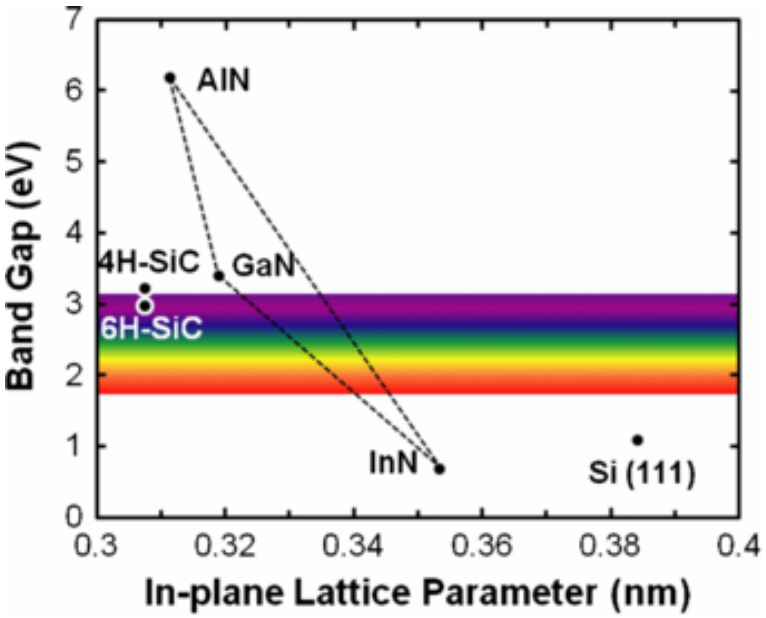

Figure 2.1.: In-plane lattice parameter and band gap for wurtzite GaN and its related alloys InGaN, InAlN, and AlGaN, covering the whole visible spectrum. Figure taken from ref. [7].

Even though the growth of III-nitride NWs is well-studied and complex axial heterostructures can be realized [27, 28, 29, 30], a systematic study of doping is necessary for a fundamental understanding and the development of different types of devices, since low resistive current injection is needed for many applications. At present, Si is used as a donor in n-type GaN NWs grown by plasma-assisted molecular beam epitaxy (PAMBE) and the influence of Si-doping on the optical and electrical properties has been studied by different techniques [9, 31, 32, 33, 34]. Quantitative analysis of the resistance in four-point probing geometry or determination of carrier concentration by thermoelectric characterization is only reported for typically longer and thicker Si-doped microwires grown by MOCVD revealing a conductivity and carrier concentration up to 2700 S/cm and $2.6 \times 10^{20}\,\mathrm{cm}^{-3}$, respectively [35, 36].
Germanium (Ge), as a shallow donor in GaN, has theoretically been predicted to have an ionization energy of 31.1 meV, which is close to the calculated value for silicon 30.8 meV [37] while the experimentally determined values for Si in GaN range between 17 meV and 28 meV [38, 39, 40] and for Ge in GaN an activation energy of 19 meV was reported [38]. Being the neighboring element of Ga in the periodic table, Ge atoms have a similar size and hence can be expected to be incorporated into the GaN lattice without significant lattice distortion. In fact, the bond length to nitrogen changes only by 1.4% compared to 5.5% for Si [41], resulting in substantially smaller lattice deformations and the absence of structural degradation in thin GaN:Ge films even for very high carrier concentrations of $4 \times 10^{20}\,\mathrm{cm}^{-3}$, as reported in ref. [42].

Recently, efficient electrostatic screening of polarization-induced internal electric fields in AlN/GaN:Ge NW heterostructure superlattices due to Ge-doping with very high carrier concentrations up to $3 \times 10^{20}\,\mathrm{cm}^{-3}$ without structural and optical degradation was observed as well [30, 43]. Therefore, Ge is studied as an alternative donor for GaN NWs grown by PAMBE on Si(111) substrates in the present work [10].
The proper determination of the carrier density is challenging for single NWs. Hall measurements on a single NW level have recently been demonstrated but require high processing effort [44, 45, 46]. Furthermore, the deduced carrier concentration can easily be overestimated by two orders of magnitude since the standard Hall theory is not applicable without corrections for NWs due to the nanosized geometry [47]. Hall measurements additionally are more difficult for highly doped semiconductors since the Hall voltage is anti-proportional to the carrier concentration. Common top gate [48, 34] and back gate [25, 49, 50, 51, 34] field-effect transistor measurements are often queried because of uncertainties determining the gate capacitance and hysteresis effects caused by interface charging [32, 52]. Another method to determine the free charge carrier density for degenerate NWs is the temperature-dependent analysis of the Seebeck coefficient, as reported in ref. [53] and [36] and will be pursued in this work.
Since no systematic relation between the concentration of incorporated Ge or Si and the conductivity of GaN NWs has been reported up to the present a systematic analysis of the influence of Ge-doping on the electrical properties of single GaN NWs will be presented in comparison to non-intentionally and Si-doped NWs in this thesis.
Following this introduction details on the growth and properties of the NWs will be presented in **Chapter 3**. The sample preparation to get access to electrical characterization on single NW level based on a process for micro- and nano-fabrication of metal contacts, established and optimized within this thesis, will be described in **Chapter 4**. Results of electrical characterization will be given in **Chapter 5**. The electrical conductivity is determined by current voltage characteristics measured in four-point geometry and the influence of the contact resistance is studied by comparative measurements in two-point geometry. An influence of the NW diameter on the conductivity and temperature dependent transport will be discussed as well. The free carrier concentration in single NWs is evaluated by analysis of the temperature-dependent Seebeck coefficient. The combination of the results allows to give an estimate of the carrier mobilities. The influence of doping on the photoluminescence properties of single NWs is also studied. In **Chapter 6** a summary of this work will be given.

Chapter 3

Gallium Nitride Nanowires

3.1. Growth and Morphology

The GaN NWs studied in this thesis were grown by plasma-assisted molecular beam epitaxy (PAMBE). For the self-assembled growth of NWs on Si(111) substrates high substrate temperatures of about 800 °C and nitrogen-rich conditions were applied [9, 54]. Doping during growth was carried out with Si and Ge.

The investigated NWs exhibit wurtzite structure and a typical length of 1 µm to 2 µm. The cross section is of hexagonal shape with diameters in the range of 30 nm to 120 nm depending on total growth time and doping concentration. A known problem related to Si-doping is the conical widening of the NWs along the growth axis for high doping concentrations [9, 31] that may result in coalescence of neighboring NWs and thus a change in electronic and optical properties. For Si- and Ge-doped samples studied in this thesis only a weak conical widening with increasing doping concentration was observed. For the Ge-doped samples, additionally a slightly increasing lateral growth rate from 3.7% to 6.8% with increasing Ge-concentration compared to 3.3% for non-intentionally doped (n.i.d.) NWs was observed [10, 54]. Due to this lateral growth, the length of the NWs is limited to avoid coalescence of the NWs. For n.i.d., Si- and Ge-doped samples a length of 2 µm could be realized. In addition, the NW density is an important parameter to control the amount of coalescence and can be influenced by the substrate temperature [54]. Since the temperature was not homogeneous across a sample during growth, areas with different degree of coalescence were be found. For electrical measurements an area with many single NWs was chosen by scanning electron microscope (SEM) analysis. Exemplarily top and side view SEM micrographs for GaN:Ge NWs with a germanium concentration[1] $[\mathrm{Ge}] = 1.4 \times 10^{20}\,\mathrm{cm}^{-3}$ are shown in **Figure 3.1**. Besides coalesced NWs several single wires with hexagonal shape are

[1] The determination of [Ge] is described in Section 3.2.

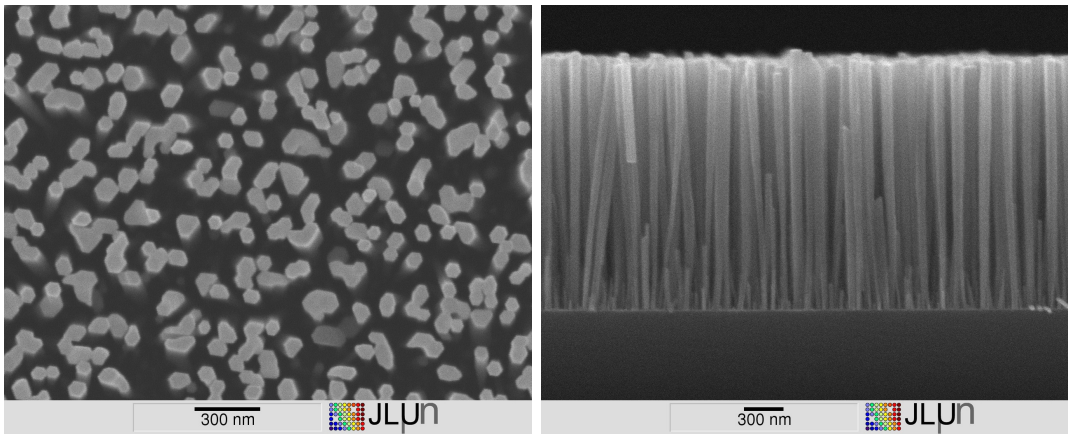

(a) Top view. (b) Side view.

Figure 3.1.: SEM micrographs in (a) top and (b) side view of 2 µm long Ge-doped GaN NWs with $[Ge] = 1.4 \times 10^{20}\,cm^{-3}$. Besides coalesced NWs several single wires with hexagonal shape are present.

present.

The NWs exhibit a very low density of structural defects, as proven by transmission electron microscopy (TEM) analysis and a line width of the near band edge (NBE) emission as small as 2 meV and 4 meV for n.i.d. and highly Ge-doped samples, respectively, determined by photo luminescence spectroscopy (PL) at a temperature of 4 K [10]. These superior structural and optical properties in comparison to thin films are a consequence of efficient strain relaxation at lateral surfaces, as discussed above [8].

3.2. Concentration of Donors

Beside n.i.d. NWs also Ge- and Si-doped GaN NWs were grown. The average Ge-concentrations [Ge] of the NW ensembles were determined by a combination of time-of-flight secondary ion mass spectrometry (ToF-SIMS) and energy dispersive X-ray spectroscopy in a transmission electron microscope (TEM-EDX) as reported in ref. [10]. In general, for a quantitative analysis by SIMS the knowledge of the relative sensitivity factors (RSF) is needed. As the latter are unknown for GaN:Ge and especially the NW geometry the SIMS data was calibrated based on the Ge-concentrations determined by EDX in TEM configuration for two samples.

In **Figure 3.2** the depth profile of the SIMS analysis of a NW ensemble with $BEP_{Ge} = 2.5 \times 10^{-10}$ mbar is exemplarily shown. Since the Ge^--signal is constant within the NW it proves homogeneous incorporation of Ge along the NW axis. The signal vanishes at the interface to the Si substrate, which is indicated by the gray area. At the interface the SiN^--signal reaches its maximum value and is attributed to a

nitridation of the substrate at the beginning of the NW-growth [9]. The increase of the Si^--signal in the region of the wires close to the substrate is due to the increasingly exposed Si substrate and to diffused Si from the substrate into the NW. The influence of Si-diffusion on the electrical properties of the NWs is discussed in **Chapter 5**. It should be noted that the intensities shown in **Figure 3.2** are raw data not corrected by RSFs and do represent concentrations.

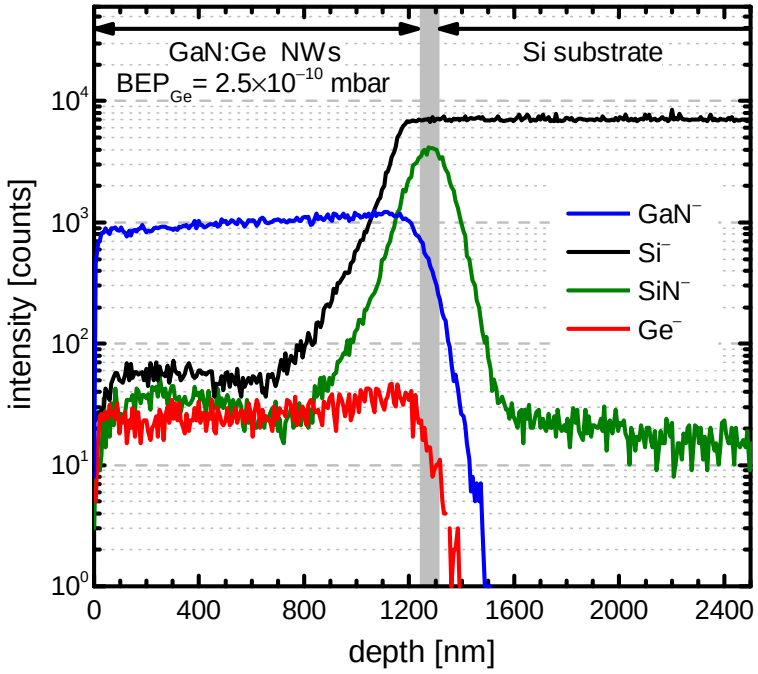

Figure 3.2.: ToF-SIMS depth-profile of a Ge-doped GaN NW ensemble. The BEP_{Ge} during growth was 2.5×10^{-10} mbar and the signals of SiN^-, Ge^-, GaN^-, and Si^- are plotted versus the sputter-depth. The gray area indicates the region of the NW/Si substrate interface. A constant Ge^--signal is present in the NW region. The increase of the Si^--signal in the region of the wires is due to the increasingly exposed Si substrate and diffused Si from the substrate into the base of the NWs. Figure based on data of ref. [10].

To get access to the real [Ge] the SIMS data was calibrated with the concentrations determined by EDX. Due to the limited resolution in EDX, only two of the highest doped samples with BEP_{Ge} larger than 5×10^{-10} mbar could be measured. Four single wires of each of these two samples grown at $BEP_{Ge} = 5 \times 10^{-10}$ mbar and $BEP_{Ge} = 1 \times 10^{-9}$ mbar were analyzed and the Ge peak-area was normalized to the Ga peak. The results were averaged exhibiting an error of about 10%. For the two investigated samples, a Ge-concentration of $1.0 \times 10^{20}\,cm^{-3}$ and $1.6 \times 10^{20}\,cm^{-3}$ were extracted, respectively. The results are shown in **Figure 3.3**. Due to the lower Ge-detection limit of SIMS compared to EDX also for the samples grown with a BEP_{Ge}

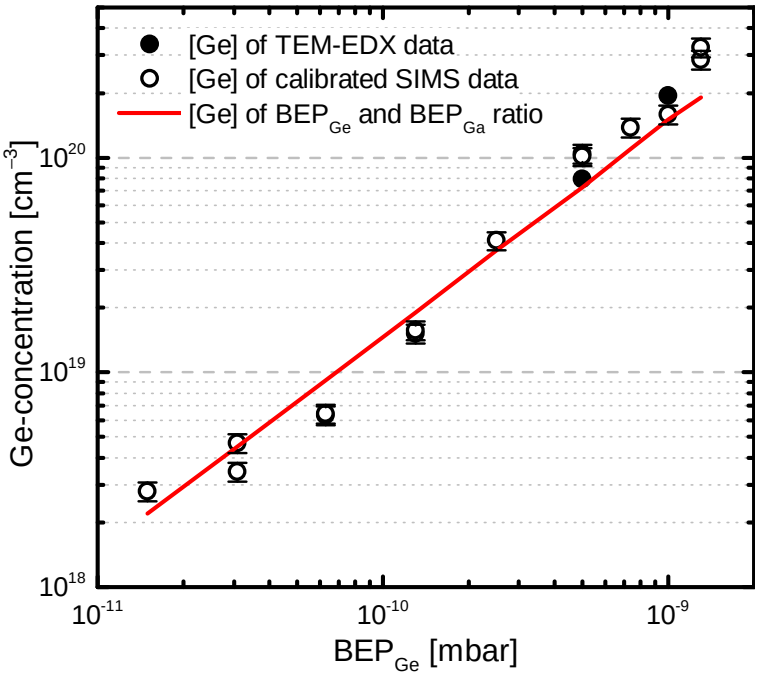

Figure 3.3.: Ge-concentration [Ge] determined by TEM-EDX measurements (filled circles) together with values of SIMS measurements after calibration (open circles) as a function of the BEP_{Ge} used during growth of the NW ensembles. The Ge-concentration increases linearly with increasing BEP_{Ge}. For comparison, the ratio of BEP_{Ga} and BEP_{Ge} is plotted as a line. Figure based on data of ref. [10].

down to 1.5×10^{-11} mbar information could be obtained, also shown in **Figure 3.3**. The Ge-concentration [Ge] increases linearly with increasing BEP_{Ge}. The filled circles represent the results of the two samples analyzed by TEM-EDX, the open circles represent the [Ge] determined from SIMS measurements after calibration. The ratio of BEP_{Ga} and BEP_{Ge} plotted as a red line fits well to the experimental results.
The Si-concentration of n.i.d., Ge-doped, and even highly Si-doped NWs could not be determined by TEM-EDX since the Ga-peak masks the Si-peak.

3.3. Influence of the Diameter

In NWs a surface band bending and a depleted region due to charge trap states at the surface occurs and has impact on the electrical and optical properties. Due to the small diameter of NWs the space charge regions can overlap and complete depletion of the NW is possible [56, 57, 58]. A scheme of the resulting lateral band profiles was suggested in ref. [55] (**Figure 3.4**). The occurrence of a conductive channel depends on the NW diameter and on the doping concentration. A radius larger than

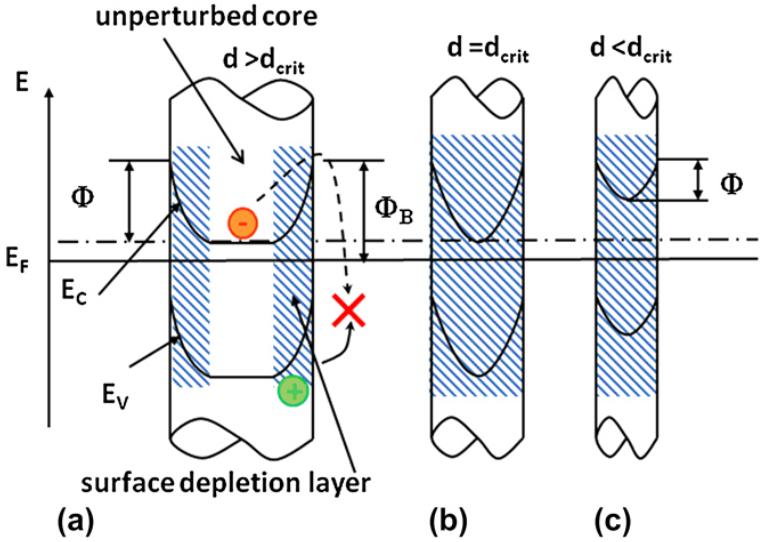

Figure 3.4.: Surface depletion layer in NWs. In the case of a NW (a) thicker than a critical diameter d_{crit} a conductive channel is present. If the diameter is (b) equal or (c) smaller than d_{crit} the NW is completely depleted. Figure taken from ref. [55].

the depletion width and an increasing donor concentration which leads to a decreasing space charge region can both result in the formation of a conductive channel inside the NW [56, 31, 57]. Consequently, the electrical properties of GaN NWs are strongly affected by surface band bending and a strong dependence of the conductance on the NW diameter is expected for undoped or moderately doped NWs. For high doping concentrations, when a conductive channel is present, only a weak influence of the NW diameter is expected.

Different groups have reported complete depletion of GaN NWs with a diameter d below the critical diameter d_{crit} of 80 nm for n.i.d. NWs with $n \approx 6 \times 10^{17}\,\text{cm}^{-3}$ and 50 nm for Si-doped NWs with $n \approx 2 \times 10^{18}\,\text{cm}^{-3}$ grown by MBE [31]. For n.i.d. NWs with $n \approx 5 \times 10^{18}\,\text{cm}^{-3}$ to $5 \times 10^{19}\,\text{cm}^{-3}$ grown by CVD the critical diameter was (35 ± 5) nm [57]. The variation of the critical diameter for n.i.d. NWs can be attributed to different residual doping concentrations depending on the specific growth method. Therefore, it is important to gain control of the NW properties by controlling the NW diameter, possibly by selective-area growth [59] using different wide openings in the mask or by changing the III/V ratio to influence the lateral growth rate or by increasing the doping concentration above the needed critical value [31, 10]. Due to the self-assembled growth of the NWs investigated here only the latter approach was followed and will be studied within this thesis.

Chapter 4

Experimental

A mandatory and challenging task of this thesis was the development, establishment and continuous improvement of an adequate processing technology for electrical contact formation on single NWs with a length of approximately 1 µm. A „mix-and-match“ process was chosen, combining photo- and electron beam lithography to achieve fast parallel patterning of large contact pads with hard masks on the one hand and well defined, exactly aligned, and individually designed nanostructures on the other hand.
This micro- and nanofabrication process chain was used to contact single NWs in different contact geometries to address the needs of the specific measurement for characterization of electrical and thermoelectrical transport properties of individual NWs.
Additionally, the establishment of different measurement setups for the electrical characterization was achieved within this work, taking the critical vulnerability of NWs to electrostatic discharges (ESD) due to their nanosized geometries into account.

4.1. Sample Preparation

The sample preparation and processing technology was carried out at the cleanroom facility „Micro- and Nanofabrication Laboratory“ (MiNa-Lab), an institution within the „Laboratory for Materials Science“ (LaMa) of Justus-Liebig-Universität Gießen. The cleanroom has a floor space[1] of 41 m^2 and is equipped with a Karl Suss MA 56 mask aligner for photolithography, a JEOL JSM 7001F thermal Schottky field emission scanning electron microscope (SEM), converted to an electron beam lithography (EBL) machine by a XENOS XeDraw2 writing system. Additionally, thermal and electron beam evaporation coating systems and equipment for pattern transfer by ion beam

[1] white room: 23 m^2, ISO 14644 class 7 | yellow room: 18 m^2, ISO 14644 class 6

dry etching and wet chemical etching are available.
For the sample preparation in this thesis photolithography and metallization was carried out using standard parameters. The identification of process parameters for the EBL and the proper alignment of the structures to obtain high overlay accuracy between NW and metal contacts, was part of the experimental challenge.
In the following a summary of the process flow will be given. Details on different steps are presented in subsequent chapters and the appendix.
A wet oxidized (insulating) 2-inch Si(100) wafer is patterned by photolithography to realize large contact pads and a set of alignment markers to maintain the requirements for an aligned EBL in a following step. After development a metal layer stack consisting of 5 nm chromium and 100 nm gold is deposited by thermal evaporation. Chromium is used as adhesion agent for the gold layer allowing bonding. Ultrasonic assisted removal of unwanted metal and resist (lift-off) is carried out in acetone. In **Figure 4.1** a patterned 2-inch wafer with 4 x 6 chips is shown. Each square chip has an edge length of 7 mm. A magnification of one chip and the centered writing field is presented in the schemes.

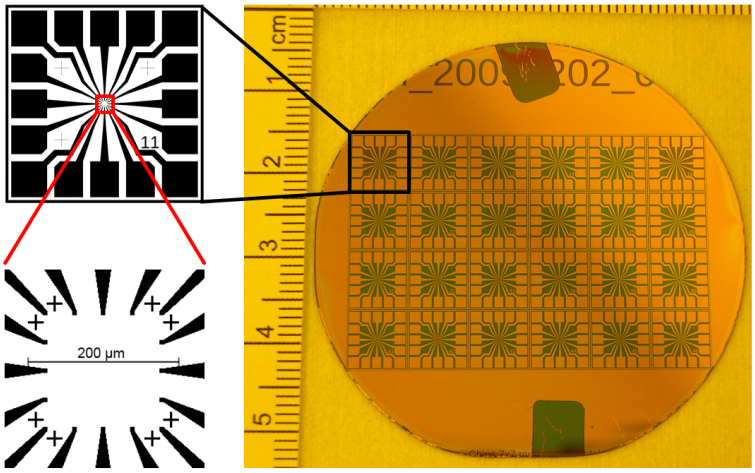

Figure 4.1.: 2-inch wafer patterned by photolithography. Each chip is 7 mm x 7 mm in size. The scheme on the left shows one chip and the centered writing field for EBL.

Subsequently, the center of each chip of the complete wafer is structured by aligned EBL, metallization (5 nm Cr / 40 nm Au) and lift-off, resulting in a finder grid with repetitive structures and labeling of every second sector for proper localization and alignment of subsequent structures. For further processing the wafer is cleaved into 6 smaller pieces, each consisting of 4 chips (2 x 2). The NWs are detached from the growth substrate by ultrasonication in isopropyl alcohol, and dispersed on the cleaved pieces. Single NWs are localized in the SEM allowing the design of individual

contacts based on the exact position of the NW in the grid-system. By means of a second aligned EBL, the layout for the contacts is transferred. For the metallization a metal layer stack consisting of 25 nm titanium and 250 nm gold is used, since this combination is known to form good Ohmic contacts to n-type GaN [60]. Single NWs contacted in different geometries are shown in **Figure 4.3** and **Figure 4.4** of the following sections. Finally the sample is cleaved to obtain single chips. After annealing for 60 s at 600 °C in vacuum (1×10^{-6} mbar) the contacts show Ohmic behavior and the samples are ready for electrical characterization.

4.2. Electron Beam Lithography

The JEOL JSM 7001F scanning electron microscope with its thermal Schottky field emission gun is a suitable tol for electron beam writing because of the combination of both high electron beam currents and high resolution.
The JEOL SEM is equipped with an electron beam writing system by XENOS Semiconductor Technologies GmbH. The writing system consists of the high speed 10 MHz pattern generator XeDraw2, the beam blanking and current measurement unit XeSwitch, and the XeMove stage monitored by a laser diffraction encoder. XeSwitch and XeMove are connected with the control unit XeBaSe and a control pad. XeSwitch additionally is connected to a Keithley 6485 PICOAMMETER to measure the electron beam current. The main components of the hardware are shown in **Figure 4.2**.

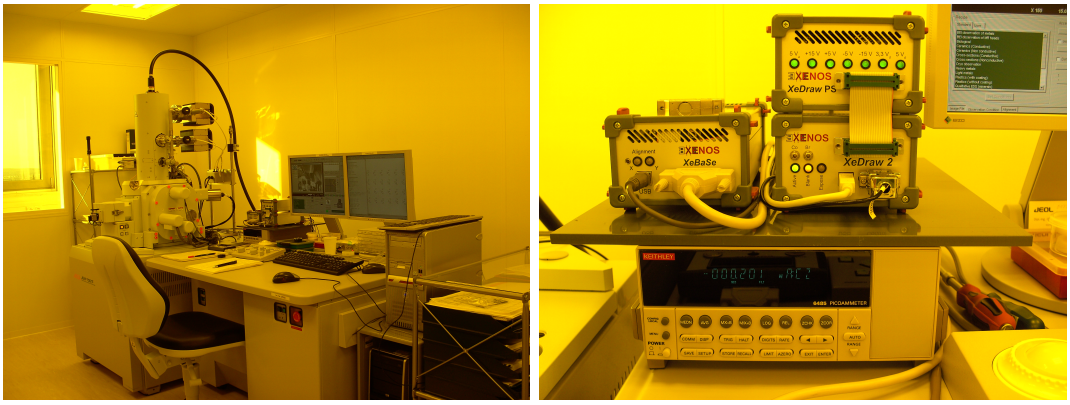

(a) SEM / EBL workplace. (b) XENOS hardware.

Figure 4.2.: SEM and EBL workplace with JEOL JSM 7001F SEM in (a) and detailed view of XENOS hardware for EBL in (b).

While for microscopy the acceleration voltage can be changed from 1 kV to 30 kV, EBL is carried out at 15 kV to reduce the „proximity effect“ (explained in the appendix) due to electron scattering.

EBL can be carried out on samples mounted to holders for the ordinary SEM stage provided by JEOL or mounted to the XeMove stage depending on the user's demands on stitching of several writing fields to realize the desired structure. Both stages allow writing in an area of $(55\,\mathrm{mm})^2$ and 2-inch wafers can be mounted.
For the work in this thesis most often the JEOL stage was used since only one writing field on a single chip and no stitching was needed. The XeMove stage was used to pattern the finder grid in an automated way without operator intervention.

4.3. Electrical Measurement Techniques

The characterization of electrical transport properties is based on measurements using metallic electrical contacts to the single NW. While processing of metal contacts was described in the previous sections, the measurement techniques to determine different material properties are described in the following.
The resistance of the metal contacts contributes to the total measured resistance, in addition the contribution of the contact resistance from the metal to semiconductor junction has to be considered. Especially for NWs the area of the metal contacts is small and hence high contact resistances can be expected, particularly for non-intentionally doped NWs. In order to exclude the influence of the contact resistance, measurements in four-point geometry were carried out as shown in **Figure 4.3** for a single NW with four contacts. Current I is injected through the outer contacts and the potential drop V between the inner two contacts is measured with a high impedance voltage meter to assure a zero-current voltage measurement. In order to exclude offsets due to thermoelectric voltages the resistance of a NW is deduced from an I-V curve.

4.3.1. Transport Measurements at Room Temperature

Measurements to characterize electrical transport properties at room temperature were carried out on a self made probe station equipped with four probe heads PH100 from Cascade Microtech[2] and tungsten probes from American Probe & Technologies with a tip radius of 2 µm. The probe station is placed inside a metal box acting as a Faraday cage and is equipped with an optical microscope.
Current-voltage characteristics in two-point and four-point geometry were carried out with a Keithley 2400 source measure unit (SMU). For the determination of the resistance a current sweep in a range from $-1\,\mu\mathrm{A}$ to $1\,\mu\mathrm{A}$ was applied. To compare

[2]Formerly known as Karl SUSS MicroTec.

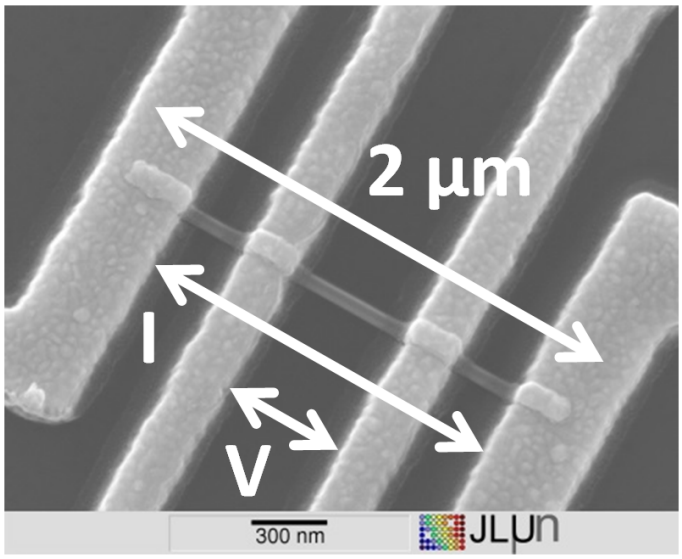

Figure 4.3.: 2 µm long single NW contacted by four individual terminals. The four-point geometry allows the measurement of the voltage V between the inner terminals caused by a current I forced through the outer contacts to determine the resistance without the influence of contact-resistances.

measurements in two- and four-point geometry the voltage was measured in both geometries. The resistance was deduced from the resulting I-V curve in order to exclude an offset due to thermoelectric voltages.
With the knowledge of the resistance R and the geometry of the analyzed segment of the NW, determined by SEM imaging, the conductivity σ was calculated according to equation 4.1 assuming a homogeneously conducting NW with a cylindrical shape with length l and diameter d.

$$\sigma = \frac{4 \times l}{R \times \pi \times d^2} \tag{4.1}$$

4.3.2. Low Temperature Transport Measurements

Transport measurements in a temperature range from 1.6 K to room temperature were carried out in an bath cryostat from Oxford Instruments cooled with liquid helium. The transport measurement setup is equipped with a superconducting magnet system generating magnetic field strengths of up to 10 T. The sample is mounted on an IC socket carrier and the pads of a chip are connected to the pins of the socket either by ball bonding or using conductive silver paint and thin metal wires. The setup consists of a stabilized DC current source (Keithley 220), picoammeter (Keithley 6485) and a nanovoltmeter (Keithley 2182). To apply different contact geometries, the setup uses a Hall matrix switching card 7065 in a switching unit 7100 (both from Keithley). A specially designed software based on National Instruments LabVIEW is used for

measurement control and data acquisition. The measurement devices were shortened during initialization and change of measuring range in order to prevent damage of the NW. The setup additionally contains a Keithley 2000 multimeter to determine the temperature of different resistive thermometers in the cryostat. A temperature control unit (ITC 4 from Oxford Instruments) is used to stabilize the temperature in the cryostat.

Temperature-dependent evaluation of the current-voltage characteristics allows an analysis of the thermal activation of free charge carriers. The Fermi distribution function $f_0(E)$, given in equation 4.2, determines the probability that an electron state of energy E is occupied as a function of temperature T.

$$f_0(E) = \frac{1}{\exp\left(\frac{E-E_F}{k_B T}\right) + 1} \tag{4.2}$$

The quantity E_F at which the Fermi distribution function is equal to $\frac{1}{2}$ is known as the Fermi energy, k_B is Boltzman's constant.

The density of electrons n, given in equation 4.3, additionally depends on the density of available electron states in the energy range between E and $E + \mathrm{d}E$ which is represented by $g(E)\mathrm{d}E$. $g(E)$ is the density of states and is given in in equation 4.4 for the three dimensional case and for parabolic bands. Here, m^* is the effective mass of a charge carrier and h is Plancks's constant.

$$n = \int_{E_C}^{\infty} f_0(E) g(E)\ \mathrm{d}E \tag{4.3}$$

$$g(E) = \frac{4\pi(2m^*)^{3/2}}{h^3}\sqrt{E - E_C} \tag{4.4}$$

Consequently n can be written as:

$$n = \frac{4\pi(2m^*)^{3/2}}{h^3}\int_0^{\infty} f_0(E) \times \sqrt{E - E_C}\ \mathrm{d}E \tag{4.5}$$

With the Fermi integral $F_{1/2}$ given in equation 4.6 the carrier density n can be written as in equation 4.7

$$F_{1/2}(x_f) = \int_0^{\infty} \frac{x^{1/2}\ \mathrm{d}x}{1 + \exp(x - x_f)} \tag{4.6}$$

$$n = 2\left(\frac{2\pi m^* k_B T}{h^2}\right)^{3/2} \frac{2}{\sqrt{\pi}}\ F_{1/2}\left(\frac{E_F - E_C}{k_B T}\right) \tag{4.7}$$

Since the Fermi integral can not be solved analytically, often the Boltzmann approximation given in equation 4.8 is used, which is only valid if $E_V < E_F < E_C$ and

$E_C - E_F > 3k_BT$.

$$n = 2\left(\frac{2\pi m^* k_B T}{h^2}\right)^{3/2} \exp\left(-\frac{E_C - E_F}{k_B T}\right) \tag{4.8}$$

According to equation 4.8 the density of free carriers depends on the temperature and the activation energy E_A as the difference between the energy of the conduction band minimum E_C and the Fermi energy E_F. The resulting resistance can be written as:

$$R(T) \propto \exp\left(\frac{E_C - E_F}{k_B T}\right) \propto \exp\left(\frac{E_A}{k_B T}\right) \tag{4.9}$$

$R(T)$ is evaluated using an Arrhenius plot, i.e. $\ln(\frac{R}{R_0})$ vs. inverse temperature. The slope of a linear fit to the values directly reveals the activation energy E_A over k_B.
For n-type semiconductors and low compensation the Fermi energy is between the donor ionization energy E_D and the conduction band minimum. Accordingly E_A in equation 4.9 musst be replaced by $E_D/2$.
NWs doped with Ge were analyzed in this way to study the influence of different doping concentrations on the thermal activation of charge carriers. The extracted activation energy is not necessarily equal to the ionization energy of the donor, since a high doping concentration shifts the Fermi energy towards the conduction band minimum and the ionization energy decreases with increasing impurity concentration as reported in ref. [61]. The lowering of the activation energy is proportional to the distance between ionized donors and is attributed to overlap of the coulomb potentials of the donors and screening of the coulomb potentials by a high concentration of free carriers. The actual donor ionization energy E_D depending on the donor concentration N_D can be described with equation 4.10. Here, S is the material specific screening factor and E_D^0 the extrapolated donor ionization energy at the donor concentration $N_D = 0$ [62].

$$E_D = E_D^0 - S \times N_D^{1/3} \tag{4.10}$$

4.3.3. Thermoelectric Measurements

To determine the charge carrier density from analysis of the temperature-dependent Seebeck coefficient, samples with a layout as shown in **Figure 4.4** were fabricated. The meandered micro-heater placed in the vicinity of the NW can be used to apply a thermal gradient along the NW. To measure the thermoelectric voltage along the NW it is contacted by two metal leads each serving as a four-point resistive thermometer. The latter were calibrated at different temperatures stabilized in the cryostat and used to determine the temperature difference along the NW. The resistances of the

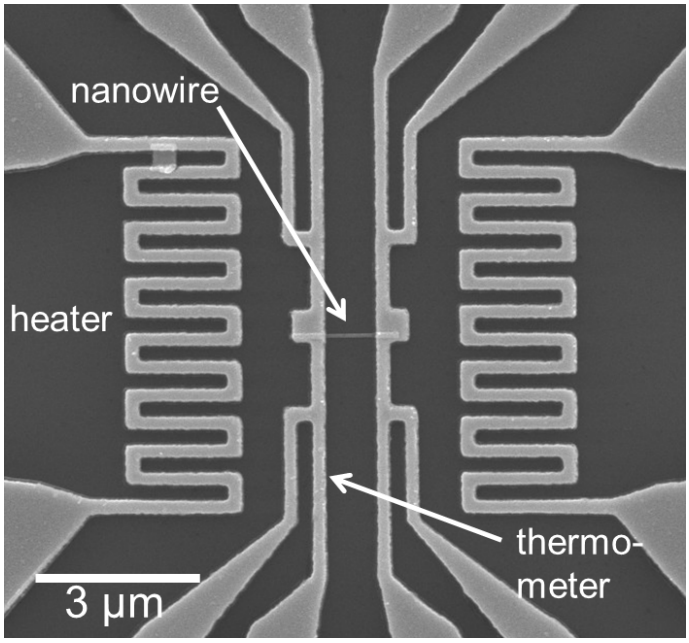

Figure 4.4.: 2 µm long NW contacted by two resistive thermometers. Each thermometer is contacted in four-point geometry. The micro heater in the vicinity is used to apply a thermal gradient along the NW.

thermometers were measured consecutively to the measurement of the thermovoltage applying the same power to the micro heater.

Usually thermocouples are used to connect macroscopic samples to determine the Seebeck coefficient in order to completely exclude the contribution of the cables to the thermovoltage. Due to the nanosized geometry of NWs this approach is not possible and therefore the thermovoltage along the gold leads connecting the hot and cold part of the NW to thermal equilibrium can not be excluded. Since the Seebeck coefficient of gold is in the order of 1.8 µV/K at room temperature and 0.8 µV/K at 80 K the influence should be small compared to the Seebeck coefficient of the NW itself with a Seebeck coefficient in the range of 120 µV/K to 20 µV/K, respectively (and it should be the same for all samples). Furthermore, if the Seebeck coefficients for different temperatures are fitted and the interest is only in the slope to determine the carrier concentration the small influence of the gold leads should be excluded.

Thermoelectric transport measurements were performed in an Oxford Instruments MicroStatHiResII flow cryostat. The temperature could be changed in a range of 5 K or 80 K to 280 K using liquid helium or nitrogen, respectively and is stabilized by an Oxford Instruments intelligent temperature control (ITC) unit. The cryostat is equipped with a ten pin electrical feed-through. The sample is glued on the sample holder using an adhesive rubber cement providing good thermal coupling to the cryostat. Electrical connections from the contact pads of the chip to the pins were

made either by ball bonding using thin gold wires or conductive silver paint and thin copper cords. For both methods the wires are connected to the pins with conductive silver paint. In **Figure 4.5** a contacted chip in the cryostat is shown.

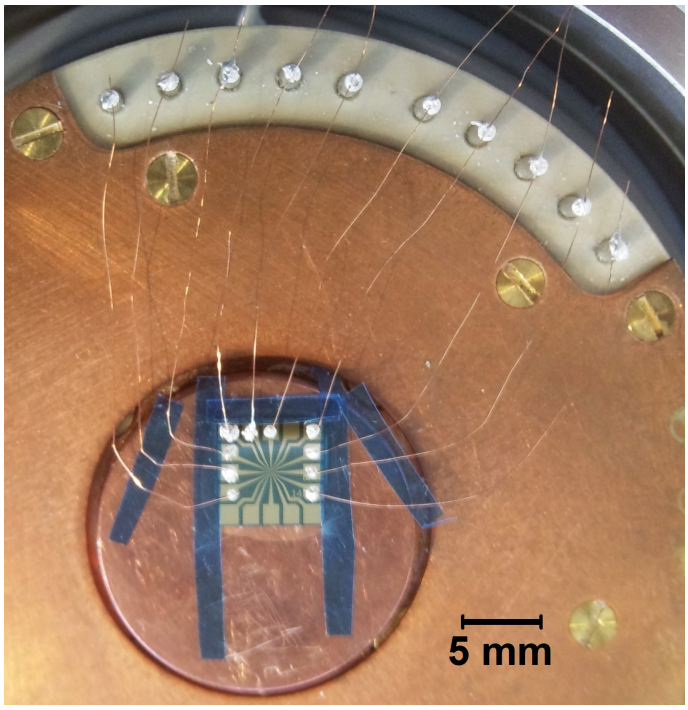

Figure 4.5.: Chip in the cryostat contacted by thin copper wires and conductive silver paint.

After contacting of the sample the cryostat is closed and evacuated to prevent heat transfer by conduction or convection. Since the cryostat is equipped with a window, which allows optical measurements, the cryostat including the window is additionally covered with aluminum foil to exclude irradiative heat transfer and guarantee constant temperature conditions during the entire thermoelectric measurements. To power the heater and measure the thermometers two Keithley 2400 SMUs are used. The thermoelectric voltage is measured with a Keithley nanovoltmeter 2182A.
The temperature-dependent measurements of the Seebeck coefficient are performed to determine the free carrier concentration n inside the NWs as described for GaN NWs in ref. [53]. The Seebeck coefficient Q is given in equation 4.11 with q as the carrier charge, in case of electrons it is the negative elementary charge $-e$.

$$Q = \frac{\pi^2 k_B^2 T}{3qE_F(T=0)} \left(\frac{\mathrm{d}\ln g(E)}{\mathrm{d}\ln E} + \frac{\mathrm{d}\ln v^2(E)}{\mathrm{d}\ln E} + \frac{\mathrm{d}\ln \tau(E)}{\mathrm{d}\ln E} \right) \tag{4.11}$$

Since the density of states is $g(E) \propto E^{1/2}$ in the parabolic band approximation and the velocity of carriers is $v^2 \propto E$ equation 4.11 can be simplified to:

$$Q = \frac{\pi^2 k_B^2 T}{3qE_F(T=0)} \left(\frac{1}{2} + 1 + \frac{\mathrm{d}\ln\tau(E)}{\mathrm{d}\ln E} \right) \tag{4.12}$$

If furthermore an energy independent scattering time τ is assumed, the last term vanishes. Since the parabolic band approximation is assumed $E_F = \frac{h^2}{8m^*}\left(\frac{3n}{\pi}\right)^{2/3}$ can be inserted in equation 4.12 and Q can be written as:

$$Q = 8\pi \left(\frac{\pi}{3}\right)^{5/3} \frac{k_B^2 m^*}{qh^2} \frac{T}{n^{2/3}} \times \frac{3}{2} \tag{4.13}$$

Finally, the carrier concentration n can be deduced if the Seebeck coefficient Q is known for a certain temperature T.

4.4. Photoluminescence Spectroscopy

The influence of doping on the optical properties was additionally analyzed by micro photoluminescence (μPL) spectroscopy using a Renishaw Raman-microscope. μPL was performed on single NW level in an Oxford MicroStatHiResII flow cryostat and a temperature of 4 K using liquid helium. The 325 nm excitation light from a HeCd laser was focused by a 20 fold UV objective (NA of 0.4) onto the NW, and the emitted PL was collected with the same objective, dispersed using a 3600 lines/mm grating in a 250 mm spectrometer, and detected with a cooled charge coupled device (CCD) camera.

Chapter 5

Results

In this chapter the results of the different electrical transport and micro photoluminescence spectroscopy measurements are presented and the influence of doping concentration on the determined properties is discussed.

5.1. Electrical Transport at Room Temperature

5.1.1. Highly Resistive Nanowires

The two-point resistance of different single non-intentionally doped (n.i.d.) NWs is shown in **Figure 5.1**. Strong variations, even for different single NWs from the same ensemble are observed. Highly resistive NWs (type 1) with a resistance above 1 MΩ (triangles) as well as conductive NWs (type 2) with a resistance in the range of 40 kΩ to 200 kΩ (squares) are found, both comparable to reported values for n.i.d. GaN NWs [56, 31, 32].

In general, the electrical properties of NWs are strongly affected by the presence of depletion layer due to surface band bending [56, 57], as discussed in **Chapter 3.3**. An increase of the donor concentration leads to a decreasing depletion width and, above a critical value, to the formation of a conductive channel inside the NW [31, 57]. As type 2 n.i.d. NWs show a measurable conductivity already for a diameter of 50 nm, a residual carrier concentration above $2.8 \times 10^{18}\,\mathrm{cm}^{-3}$ can be estimated according to the model proposed in ref. [56], which is significantly higher than the Mott density of $1.6 \times 10^{18}\,\mathrm{cm}^{-3}$ for bulk GaN [62]. The actual carrier concentration of $9.1 \times 10^{18}\,\mathrm{cm}^{-3}$ for another conductive n.i.d. NW from the same ensemble, deduced from temperature-dependent Seebeck coefficient measurements, reported in **Chapter 5.3**, was higher than this estimation for a lower limit.

The origin of the unexpected high carrier concentration can be attributed to oxygen impurities and to diffusion of silicon from the substrate into the NWs. Furtmayr *et al.*

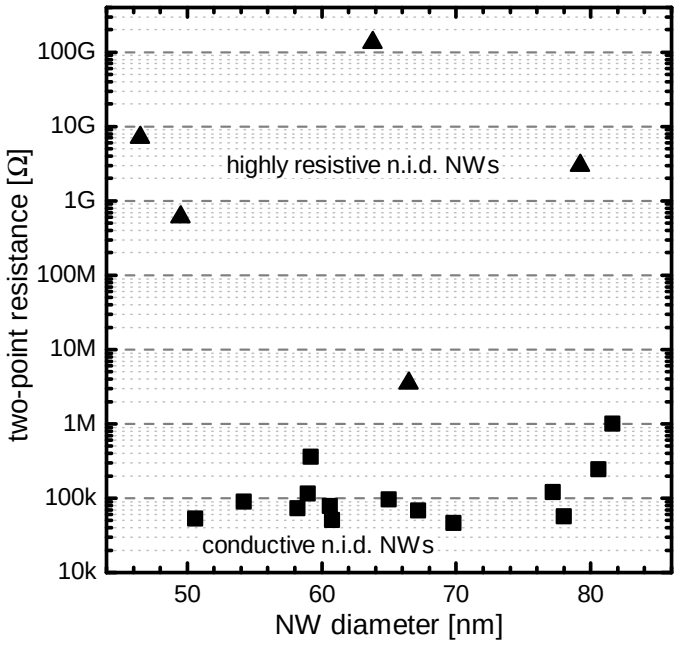

Figure 5.1.: Two point resistance of highly resistive (triangles) and conductive (squares) n.i.d. NWs as a function of their diameter.

observed a high concentration of some percent of Si due to diffusion very close to the interface between NW base and Si growth substrate by electron energy loss spectroscopy (EELS) [9], cf. **Figure 5.2**. Due to the limited resolution of EELS to Si concentrations above 1% a determination of very low Si concentrations in the NW, comparable to typical doping concentrations, was not possible far away from the interface.

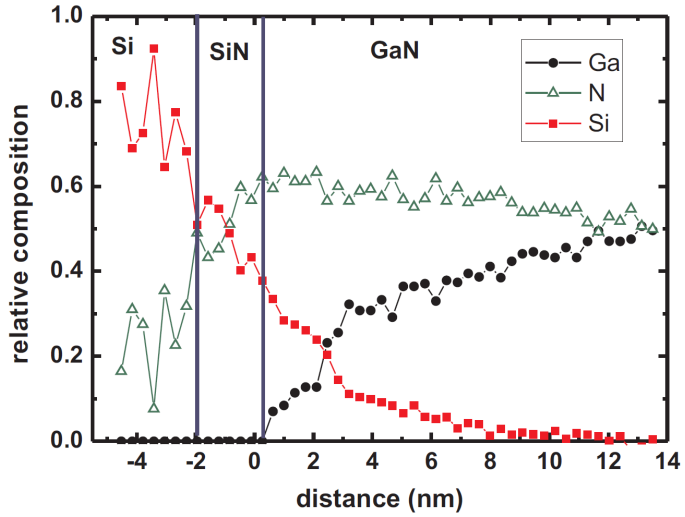

Figure 5.2.: Relative composition of atoms at the NW interface to the Si substrate determined by electron energy loss spectroscopy (EELS). Figure taken from ref. [63].

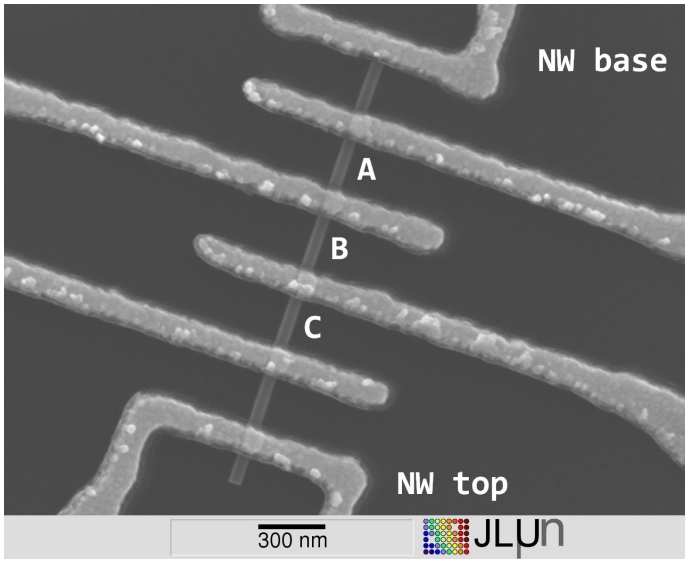

Figure 5.3.: Single 2 µm long n.i.d. NW contacted with six terminals to measure the resistance at three segments A, B, and C in four-point geometry.

As presented in **Chapter 3.2** the determination of the germanium concentration [Ge] in doped NWs was carried out by ToF-SIMS calibrated by TEM-EDX. For doped and n.i.d. NWs a high Si^--signal rising even 500 nm before the interface to the substrate was observed (cf. **Figure 3.2**). Possibly a part of this Si^--signal could be a measurement artifact related to the NW morphology, i.e. the exposed Si substrate between the NWs, or can be attributed to Si diffusion out of the substrate into the NW.

In order to clarify the occurrence of Si diffusion samples with 2 µm long n.i.d. NWs contacted by six individual terminals were prepared, as shown in **Figure 5.3**. This layout allows four-point measurements at three different segments A, B, and C along one NW. In **Figure 5.4** the obtained conductivity for nine different NWs (each NW is represented by one type of symbol) depending on the distance of the measured NW segment's center to the NW base is shown on a logarithmic scale. A decrease of the conductivity over one decade from 81 S/cm to 9 S/cm when the distance to the NW base is doubled from approximately 600 nm to 1300 nm is observed. The measured conductivities for different NWs at the same segments, i.e. similar distances to the base, show only small variations compared to the change of conductivity for the individual segments A, B, and C, thus different distances to the NW base. Because the diameter is almost constant along the NW (not shown here for all, cf. **Figure 5.3**) such a change of conductivity cannot be explained by the NW geometry. Furthermore, a conical widening of the NW from the base to the top would have a contrary effect. Therefore the increased conductivity at the base can be attributed to diffusion of

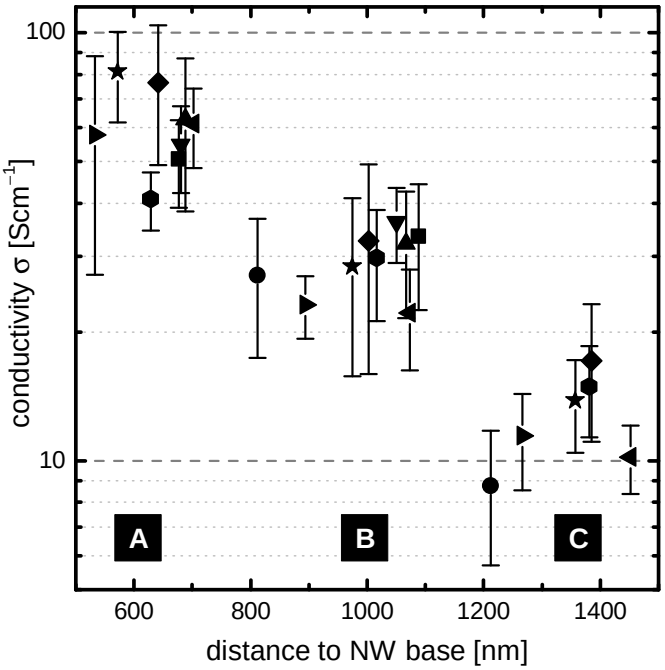

Figure 5.4.: Conductivity as a function of the distance of the respective NW segment to the NW base for nine different single n.i.d. NWs. Each NW is resembled by one type of symbol. The three individual segments are marked by A, B, and C in accordance with Figure 5.3

Si from the Si(111) substrate into the NW. The gradual Si-doping in addition to a doping of impurities as oxygen explains conductive n.i.d. NWs down to a diameter of 50 nm, as reported above.

In the case of PAMBE grown GaN n.i.d. NWs on Si(111) substrates a comparison of the electrical properties to other groups is questionable since the measured distance to the NW base is not known. Furthermore different growth temperatures can result in different diffusion profiles, thus conductivity and carrier concentration might also differ.

Since even at a distance of 600 nm to the base of the n.i.d. NWs the conductivity of about 60 S/cm is significantly smaller than the conductivity of the lowest Ge-doped NWs (142 S/cm) at the center of the NW (1000 nm to the base), the effect of Si diffusion should not have a significant effect of co-doping for the Ge-doped NWs. In fact the average conductivity of n.i.d. NWs is one order of magnitude smaller than the conductivity of Ge-doped NWs, as reported in **Chapter 5.1.3**.

5.1.2. Influence of Contact Resistance

To analyze the contact resistance of individually contacted NWs current voltage (I-V) measurements in two-point and four-point geometry were compared for n.i.d. and Ge-doped NWs. **Figure 5.5** shows the deduced resistances of the middle segment of in total 36 conductive single NWs in two-point (R_{2P}, open symbols) and four-point geometry (R_{4P}, filled symbols) on a logarithmic scale. The measurement error is smaller than the size of the symbols. For clarity, the x-axis is divided into five sectors representing the different Ge-concentrations [Ge] from 0 (n.i.d.) to $3.3 \times 10^{20}\,\mathrm{cm}^{-3}$ of the respective NW ensemble obtained by ToF-SIMS as reported in **Chapter 3.2**. Highly resistive n.i.d. NWs (type 1) are not included, since their resistance measured in four-point geometry is almost the same as in two-point geometry. For these NWs the influence of the contacts to the resistance can not be determined.

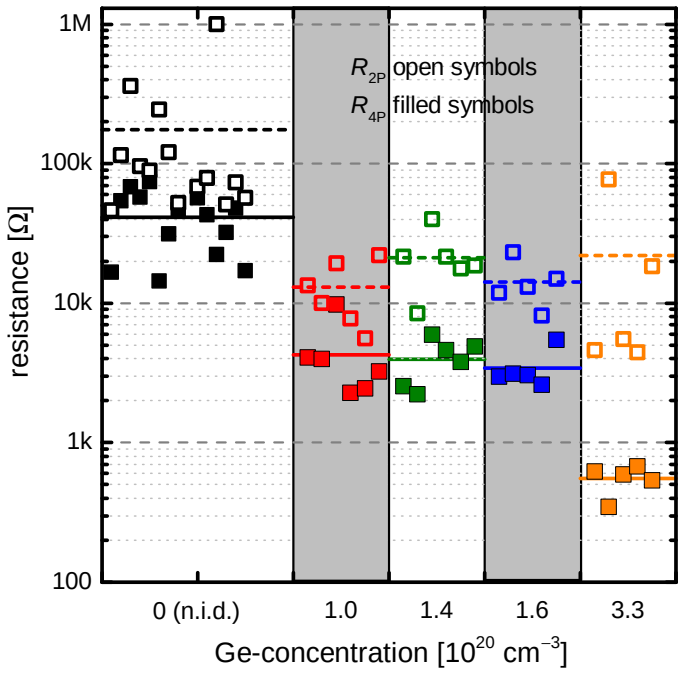

Figure 5.5.: Resistance of middle segments in individual NWs measured in two-point (R_{2P}: open symbols) and four-point (R_{4P}: filled symbols) geometry for 36 conductive NWs with different Ge-concentrations. The x-axis is divided into five sectors corresponding to the Ge-concentration of the respective NW ensemble. Vertically aligned R_{2P} and R_{4P} values of equal color correspond to the same NW. Dashed (solid) lines show the average value of R_{2P} (R_{4P}).

The values for R_{2P} show strong wire-to-wire variations and an overall decrease by more than two orders of magnitude with increasing [Ge]. However, the average values (dashed lines) do not exhibit a clear trend. In contrast, the results for R_{4P} show

significantly less variations and the mean values (solid lines) decrease systematically over two decades from 41 kΩ to 552 Ω with increasing [Ge]. Hence, the strong fluctuations of R_{2P} are caused by variations in the contact resistance. The latter was calculated from the data in **Figure 5.5** and turned out to be in the same order of magnitude as the four-point resistance of the middle segment of each NW itself, as shown in **Figure 5.6**. Hence, four-point measurements are inevitable for reliable electric characterization of single NWs.

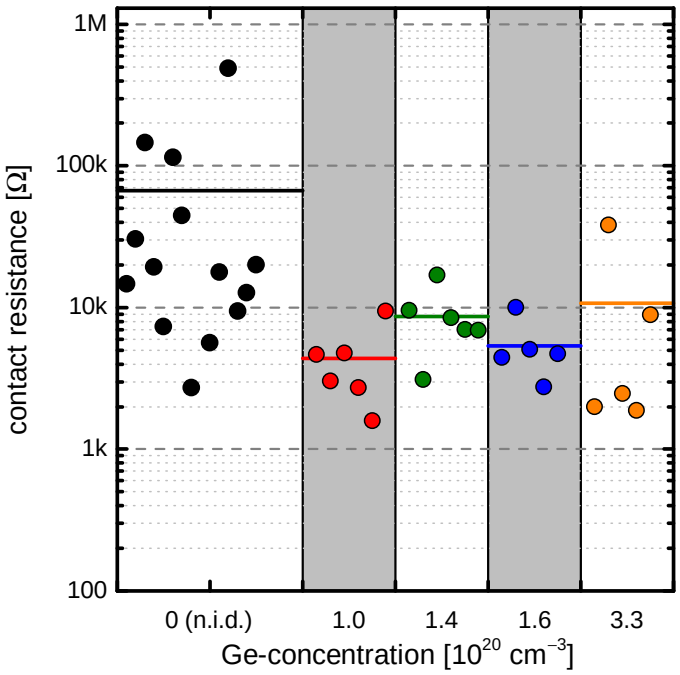

Figure 5.6.: Contact resistance as half difference of two-point (R_{2P}) and four-point (R_{4P}) resistances. The x-axis is divided into five sectors corresponding to the Ge-concentration of the respective NW ensemble.

5.1.3. Influence of Ge-Doping on the Conductivity

As presented above, a higher Ge-concentration in the NW leads to significantly lower resistance compared to n.i.d. NWs. To obtain the electrical conductivity σ, which excludes the geometry of the NW, the NWs have been approximated to be of cylindrical shape. The individual diameter and length of the electrically measured middle segment of the NW was determined by SEM analysis.

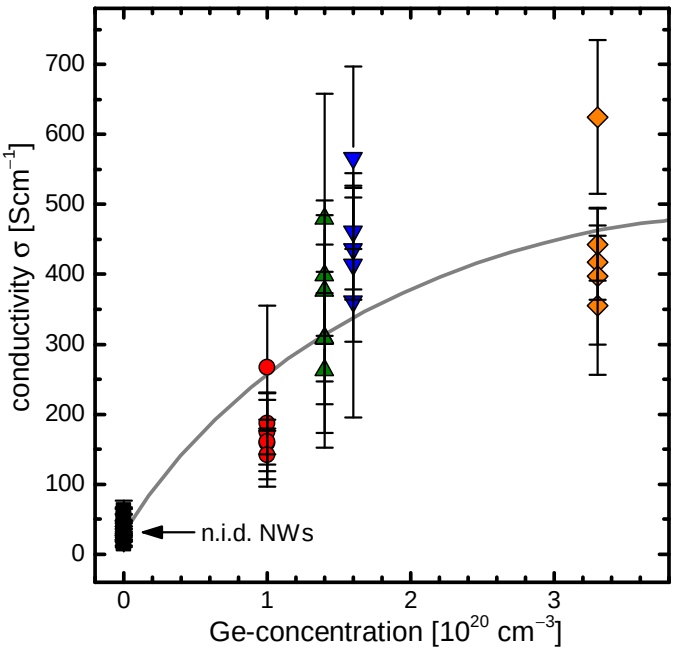

Figure 5.7.: Conductivity of 36 NWs as a function of the Ge-concentration of the respective NW ensemble. The conductivity was obtained from the four-point resistance considering the individual NW geometry. The error bars are dominantly caused by the uncertainties in the NW geometry determined from SEM images. The line is a guide to the eye.

The results in **Figure 5.7** show a continuous increase of the conductivity from 35 S/cm to 400 S/cm for an increasing [Ge] up to 1.6×10^{20} cm^{-3}. For higher doping concentrations up to [Ge] $= 3.3 \times 10^{20}$ cm^{-3} the conductivity saturates at an average value around 450 S/cm. Possible reasons for the saturation are a decreasing carrier mobility caused by a high density of ionized donors, self-compensation, or electrically inactive incorporation of Ge. A maximum conductivity of 625 S/cm for one NW of the highest doped ensemble was observed. The large error bars are dominantly caused by the uncertainties determining the NW geometry from the SEM images.
The wire-to-wire fluctuation can be caused by variations in the concentration of active Ge donors, as suggested also in ref. [10] or by mobility variations due to different densities of structural defects. Since the diameter of the NW was used to calculate

the conductivity and an influence of a possible depletion region was neglected the values represent a lower limit. Nevertheless, the obtained values are in very good agreement with reports about Ge-doped thin films with conductivities is the range from 30 S/cm to 1500 S/cm for carrier concentrations of $2 \times 10^{18}\,\mathrm{cm}^{-3}$ to $2 \times 10^{20}\,\mathrm{cm}^{-3}$, respectively [42, 64].

5.1.4. Influence of the Diameter on the NW Conductivity

The dependence of the conductivity on the NW diameter for different Ge-concentrations is shown in **Figure 5.8**. For n.i.d. NWs of type 2 a systematic increase of the conductivity with increasing diameter is observed, in agreement with the results reported in refs. [56] and [57]. An increase of the donor concentration above a critical value leads to a decreasing depletion width and the formation of a conductive channel inside the NW [31, 57]. Hence, a strong dependence of the conductivity on the NW's diameter is expected for undoped or moderately doped NWs while for high doping concentrations only a weak dependence is expected. Accordingly, for all Ge-doped NWs investigated here the influence of the depletion region on the conductivity can be neglected. Furthermore, as type 2 n.i.d. NWs show a measurable conductivity already for a diameter of 50 nm, a residual carrier concentration above $2.8 \times 10^{18}\,\mathrm{cm}^{-3}$ can be estimated, as reported in **Chapter 5.1.1**. For thick n.i.d. NWs, when the depletion region can be neglected in respect to the conductive channel, a saturation of the conductivity around 100 S/cm can be expected at a diameter above 90 nm as indicated by the tapered gray shaded area in **Figure 5.8**.

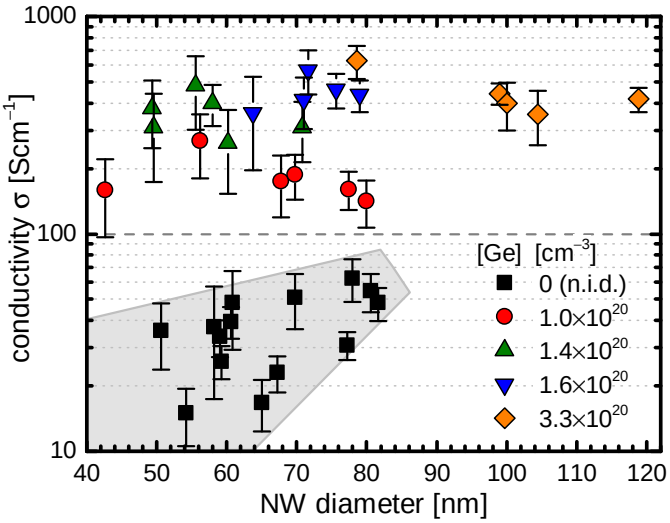

Figure 5.8.: Conductivity for NWs with different Ge-concentration as a function of the NW diameter. The gray shaded area depicts the region spanned by n.i.d. NWs.

5.2. Temperature-dependent Transport

To investigate the donor ionization energy temperature-dependent resistivity measurements between 1.6 K to 280 K were carried out. Selected NWs with different conductivities of the NW ensembles with no intended doping, a [Ge] of $1.4 \times 10^{20}\,\mathrm{cm}^{-3}$ and $1.6 \times 10^{20}\,\mathrm{cm}^{-3}$ were analyzed. For all investigated NWs only a weak influence of the temperature and an almost constant resistivity at temperatures below 10 K was found, as exemplarily presented in **Figure 5.9**. The extracted activation energy be-

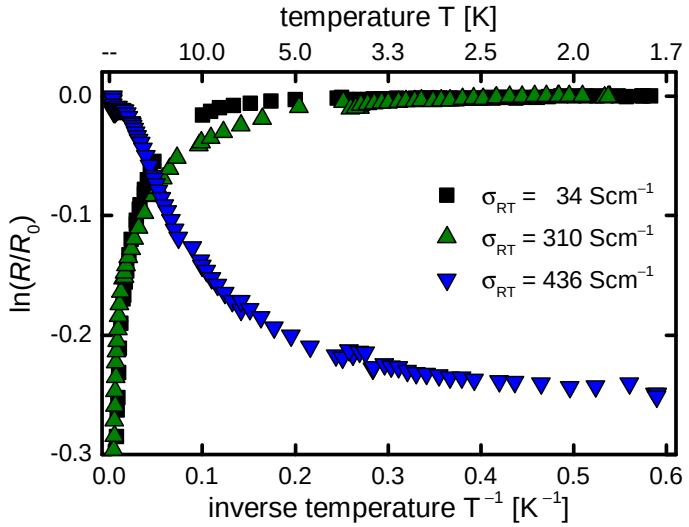

Figure 5.9.: Arrhenius plot of normalized four-point resistance $(R(T)/R_0(280K))$ for three NWs with different conductivities.

tween 80 K and 280 K for the NW with the conductivity of 310 S/cm is approximately 5 meV. This value is significantly lower than the ionization energy of Ge in the case of low doping concentrations (19 meV for $n = 3 \times 10^{17}\,\mathrm{cm}^{-3}$ [38]) and indicates the formation of an impurity band due to high concentrations of incorporated Ge atoms [61, 65]. As introduced in **Chapter 4.3.2** the lowering of the activation energy is attributed to an overlap of the coulomb potentials of the donors and screening of the coulomb potentials by a high concentration of free carriers. Based on the ionization energy of 19 meV for $n = 3 \times 10^{17}\,\mathrm{cm}^{-3}$ observed by Götz *et al.* [38] and a screening factor $S = 2.1 \times 10^{-5}$ meVcm [66] the carrier concentration in the NWs can be roughly estimated to $2.4 \times 10^{18}\,\mathrm{cm}^{-3}$ using equation 4.10. This value is almost the same as the lower limit deduced in **Chapter 5.1.1** but significantly lower than the carrier concentrations determined in **Chapter 5.3**. Associated with this estimation, it should be noted that the determination of the activation energy is rather sensitive to the evaluated temperature range. Therefore this technique is inappropriate to determine quantitatively reliable values for the charge carrier concentration.

For the investigated NW with the highest conductivity, a positive temperature coefficient of the resistivity was observed, i.e. metallic behavior, further confirming the high donor concentration in Ge-doped GaN NWs.
Overall, the temperature-dependent measurements confirm the high doping concentrations indicated by the independence of the conductivity of GaN:Ge NWs on the NW diameter.

5.3. Carrier Concentration

To determine the charge carrier concentration of individual GaN NWs the approach reported for degenerate n.i.d. GaN NWs with a carrier concentration of $6.6 \times 10^{19}\,\mathrm{cm}^{-3}$ in ref. [53] and Si-doped GaN microwires with a carrier concentration of $6 \times 10^{19}\,\mathrm{cm}^{-3}$ and $2.6 \times 10^{20}\,\mathrm{cm}^{-3}$ [36] based on temperature-dependent measurements of the Seebeck coefficient was pursued. Using the test structures presented in **Figure 4.4** the transient thermoelectric voltage of individual NWs was measured, as described in **Chapter 4.3.3**. The voltage instantaneously increases with the heating power steps as exemplarily shown for a temperature of 282 K and a NW of the ensemble with $[\mathrm{Ge}] = 1.0 \times 10^{20}\,\mathrm{cm}^{-3}$ in **Figure 5.10**.
The evaluation of the steps in the thermoelectric voltage reveals a linear increase from $-40\,\mu\mathrm{V}$ to $250\,\mu\mathrm{V}$ for heater powers up to 5 mW and a corresponding temperature difference up to 3.5 K along the NW as depicted in **Figure 5.11**. The offset at $\Delta T = 0$ is caused by thermoelectric voltage in the cables. As only the slope of the linear relation is evaluated it does not interfere with the extracted results for the Seebeck coefficient. Evaluation of the slope yields a Seebeck coefficient of $Q = -82.3\,\mu\mathrm{V/K}$ at the average temperature of 282 K. This Seebeck coefficient is comparable to results reported for n-type GaN wires [53, 36] and GaN thin films [67] with carrier concentrations above $1 \times 10^{19}\,\mathrm{cm}^{-3}$.
Following this method the Seebeck coefficients for one type 2 n.i.d. NW and two Ge-doped NWs from ensembles with $[\mathrm{Ge}] = 1.0 \times 10^{20}\,\mathrm{cm}^{-3}$ and $[\mathrm{Ge}] = 1.6 \times 10^{20}\,\mathrm{cm}^{-3}$, respectively, were determined at different temperatures in the range of 80 K to 280 K, as presented in **Figure 5.12**. A linear decrease of the Seebeck coefficients with increasing temperature was observed. The negative sign of Q indicates that the carrier transport in all investigated GaN NWs is contributed by electron diffusion, reflecting that the NWs are n-type semiconductors. The absolute value of the extracted slope decreases with increasing [Ge] as expected for higher carrier concentrations. The linearity is maintained for temperatures down to 5 K, as exemplarily shown for the n.i.d. NW in **Figure 5.12**. This further confirms a degenerate doping level of all investigated NWs

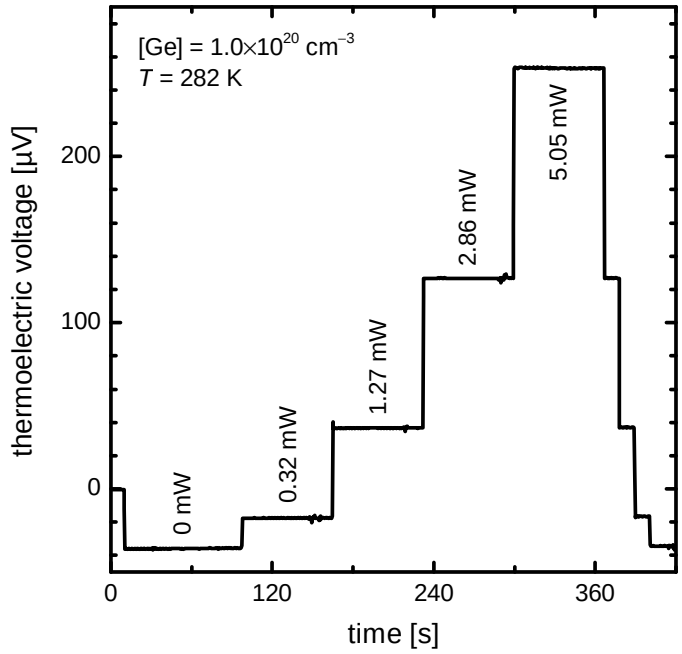

Figure 5.10.: Transient thermoelectric voltage for different stepwise increased heating powers for a NW with $[\mathrm{Ge}] = 1.0 \times 10^{20}\,\mathrm{cm}^{-3}$ at $T = 282\,\mathrm{K}$.

due to doping concentrations above the Mott density in accordance with the results of the temperature-dependent resistivity measurements (cf. **Chapter 5.2**) and the weak dependence of the conductivity on the NW diameter (cf. **Chapter 5.1.4**).
Hence, assuming parabolic bands and a constant effective mass, which is valid for carrier concentrations up to $1 \times 10^{20}\,\mathrm{cm}^{-3}$ [68, 69], and an energy-independent scattering time a lower limit for the carrier concentration n can be estimated adapting equation 5.1 derived from semi-classical Mott relation [53].

$$n = \sqrt{\left(\frac{\pi^2 k_B^2 m^*}{(3\pi^2)^{2/3} q\hbar^2}\frac{T}{Q}\right)^3} \tag{5.1}$$

Here, k_B is the Boltzmann constant, q the elementary charge, $\hbar$ reduced Planck's constant, $m^* = 0.231 \times m_e$ the electron density of states effective mass [68, 69], T the temperature, and Q the Seebeck coefficient.
Using this equation carrier concentrations between $9.1 \times 10^{18}\,\mathrm{cm}^{-3}$ and $5.5 \times 10^{19}\,\mathrm{cm}^{-3}$ were obtained for the five different NWs as summarized in **Table 5.1**. The used method to evaluate the slope (linear regression with intercept) instead of analyzing just one Seebeck coefficient at a certain temperature, as carried out in ref. [36], benefits from the exclusion of uncertainties in the determination of the absolute temperature, since the temperature T as a parameter in equation 5.1 has a significant influence

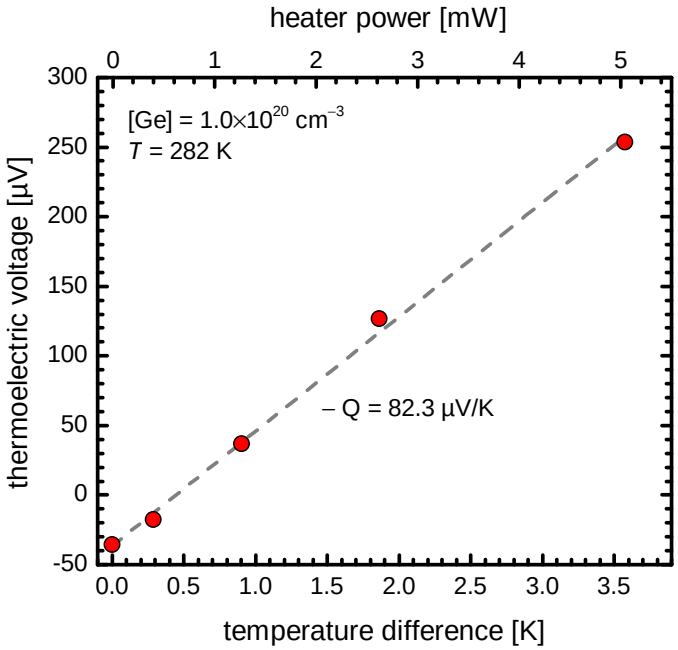

Figure 5.11.: Thermoelectric voltage as a function of heater power and resulting temperature difference for a NW with $[\mathrm{Ge}] = 1.0 \times 10^{20}\,\mathrm{cm}^{-3}$ at $T = 282\,\mathrm{K}$.

on the calculation. The error in the determination of the slope is small and can be neglected in comparison to the uncertainty in the effective mass, which has a more significant influence on the results. The corrections suggested in ref. [36] to address the energy-dependent relaxation time can be neglected in comparison to the uncertainties in the temperature and effective mass.

NW	$\mathrm{BEP_{Ge}}$ $[10^{-9}$ mbar]	[Ge] $[10^{20}$ cm$^{-3}]$	slope $[\mu\mathrm{V/K}^2]$	n $[10^{19}$ cm$^{-3}]$
1	0 (n.i.d.)	0 (n.i.d.)	−0.53	**0.91**
2	0.5	1.0	−0.31	**2.05**
3	0.5	1.0	−0.27	**2.57**
4	1.0	1.6	−0.20	**4.11**
5	1.0	1.6	−0.16	**5.53**

Table 5.1.: Beam equivalent pressure $\mathrm{BEP_{Ge}}$ and Ge-concentration [Ge] of the respective NW ensemble, slope deduced from graph in Figure 5.12 and calculated carrier concentration n for five different doped single GaN NWs.

The extracted values for n systematically increase with increasing Ge-concentration. They also reflect the wire-to-wire variations observed in conductivity, since the ratio of n and [Ge] varies in the range of 20% to 35% for the investigated single NWs in relation

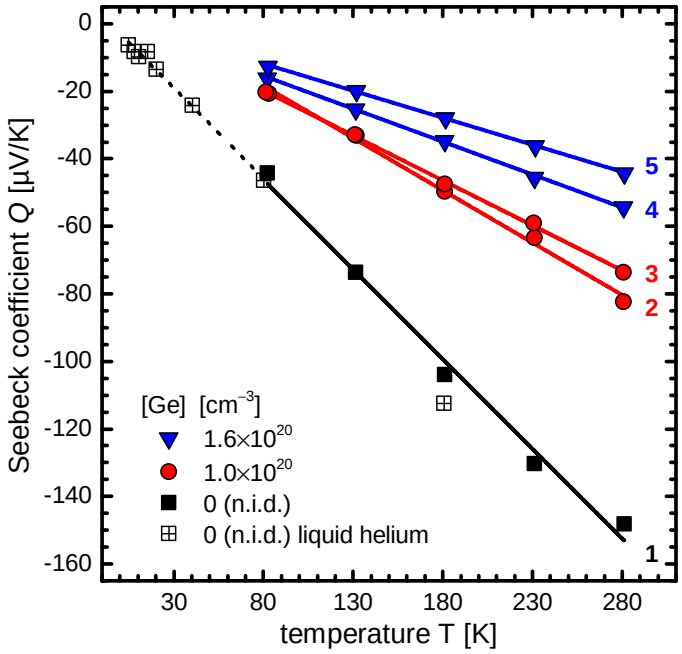

Figure 5.12.: Seebeck coefficient as a function of temperature for one n.i.d. and four Ge-doped GaN NWs. The n.i.d. NW was measured down to a temperature of 5 K using liquid helium.

to the respective ensemble. The extracted carrier concentrations and the conductivities obtained for single NW of the same ensembles are in very good agreement with data reported in literature [57, 42, 64]. The high carrier concentration of the n.i.d. NW can be attributed to residual oxygen and Si donors [9] as discussed in **Chapter 5.1.1**. All carrier concentrations exceed the Mott density, which is in accordance with the prior results of the diameter-independence and weak temperature-dependence of the conductivity discussed above.

5.4. Carrier Mobility

Based on the results obtained for the conductivity in **Chapter 5.1.3** and the charge carrier density in **Chapter 5.3** the electron mobility μ_e can be estimated. Since both measurement techniques were carried out on different single NWs of the same ensemble, for the calculation every single conductivity from **Figure 5.7** for NWs with $[\mathrm{Ge}] = 1.0 \times 10^{20}\,\mathrm{cm}^{-3}$ and $[\mathrm{Ge}] = 1.6 \times 10^{20}\,\mathrm{cm}^{-3}$ was combined with both corresponding charge carrier concentrations from **Table 5.1** of the respective NW ensemble with the same [Ge]. The results are presented in **Figure 5.13**.
The mobility varies in the range from $10\,\mathrm{cm}^2/\mathrm{Vs}$ to $43\,\mathrm{cm}^2/\mathrm{Vs}$ for the n.i.d. NWs, $34\,\mathrm{cm}^2/\mathrm{Vs}$ to $81\,\mathrm{cm}^2/\mathrm{Vs}$ for NWs with $[\mathrm{Ge}] = 1.0 \times 10^{20}\,\mathrm{cm}^{-3}$, and $40\,\mathrm{cm}^2/\mathrm{Vs}$ to

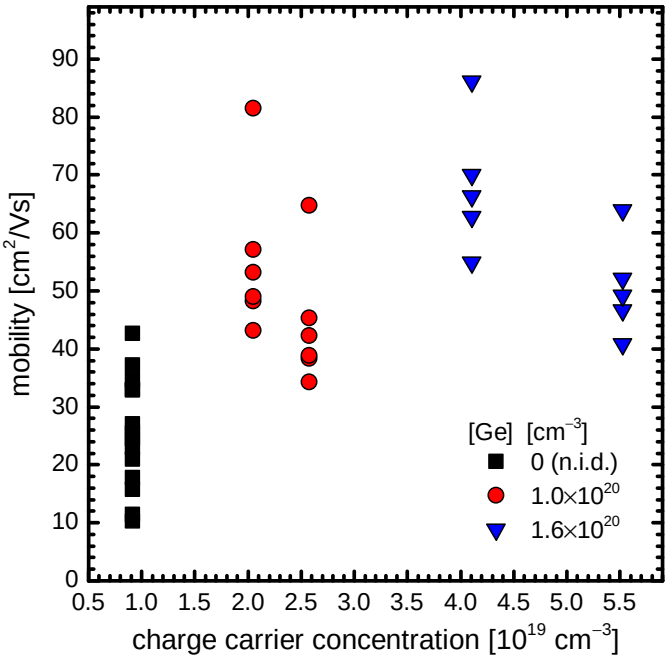

Figure 5.13.: Electron mobility as a function of the charge carrier concentration.

86 cm^2/Vs for NWs with $[Ge] = 1.6 \times 10^{20}\,cm^{-3}$ being reasonable compared to reported values for NWs and thin films [70, 25, 42, 50, 71, 72, 51, 57, 64, 36]. By first excluding the n.i.d. NWs, the conductivity seems to be constant around 50 S/cm, independent on the charge carrier concentration, whereas a slight decrease with increasing carrier concentration is expected [73]. The smaller mobility for the n.i.d. NWs can be explained by the fact, that the conductivity was calculated with the NW diameter neglecting an influence of the depletion region, as discussed in **Chapter 5.1.4**. Therefore, a higher conductivity and mobility for n.i.d. NWs can be expected in comparison to this calculated lower limit. Furthermore, the carrier concentration was determined for a whole n.i.d. NW, contacted on base and top of the NW, whereas the conductivities were determined for the middle segments of the NWs due to the four-point geometry, but as reported in **Chapter 5.1.1** a significant change of the conductivity is observed along n.i.d. NWs.
Only combined measurements of both properties on a specific segment of the same single NW will result in reliable values for the carrier mobility.

5.5. Photoluminescence Spectroscopy

The five single NWs that were analyzed by Seebeck coefficient measurements, with carrier concentrations from $9.1 \times 10^{18}\,cm^{-3}$ to $5.5 \times 10^{19}\,cm^{-3}$ were analyzed by μPL

at $T = 4\,\mathrm{K}$.

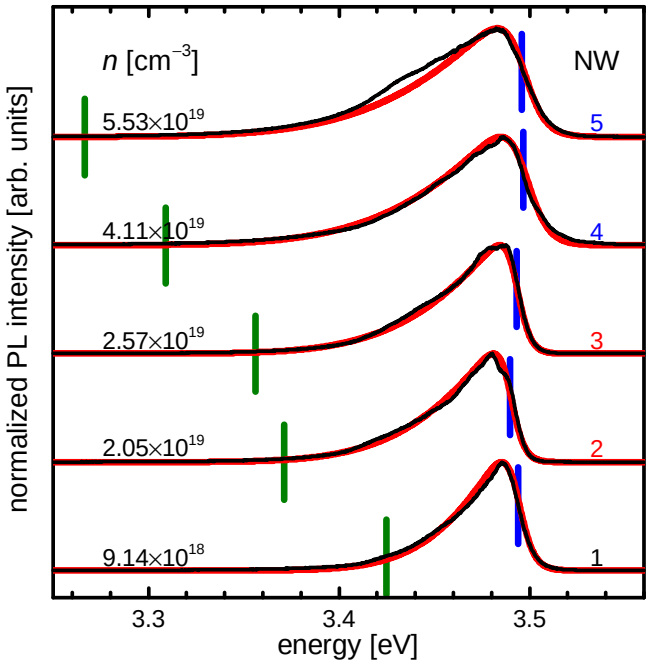

Figure 5.14.: Micro photoluminescence spectra of five single NWs at $T = 4\,\mathrm{K}$ with different carrier concentrations (determined by temperature-dependent analysis of the Seebeck coefficient). The spectra are normalized and vertically shifted for clarity. Experimental data are plotted in black, the modelled luminescence line shapes in red. The vertical green and blue lines mark the positions of $E_{\mathrm{gap}} + \Delta E_{\mathrm{BGR}}$ and $E_{\mathrm{gap}} + \Delta E_{\mathrm{BGR}} + \Delta E_{\mathrm{BMS}}$, respectively.

The spectra of all NWs, shown in **Figure 5.14**, are dominated by a sharp near band edge emission around 3.485 eV. While the full width of half maximum (FWHM) of the emission broadens only slightly from 35 meV to 70 meV with increasing carrier concentration, no spectral shift is observable even for the highest doped sample. This is remarkable since for similar Ge-doped NW ensembles the near band edge emission was observed at 3.472 eV [10]. Furthermore, in single NW μPL Schoermann *et al.* observed emissions in a range from 3.46 eV to 4.90 eV for various wires. All single NWs analyzed here seems to correspond to *category D* introduced in ref. [10]. Whether it is coincidence or that the sample preparation, or the temperature cycling during the temperature-dependent measurements of the Seebeck coefficient has an influence on the optical properties, can not be clarified.

Anyhow, the observed behavior of a constant peak position independent on the carrier concentration, can be explained by a compensation of a blue shift due to band filling effects known as Burstein-Moss shift (BMS) by band gap renormalization (BGR) due to many body effects as recently reported in ref. [69] for GaN:Si and GaN:Ge samples

with carrier concentrations up to $1 \times 10^{19}\,\mathrm{cm}^{-3}$. A lowering of the fundamental band gap energy of the semiconductor is expected to be dominated by electron electron and electron ion interaction.
Fits to the experimental line shapes according to the model used in ref. [69] are plotted in red in **Figure 5.14**. The position of the renormalized band gap given by $E_{\mathrm{gap}} + \Delta E_{\mathrm{BGR}}$ and the Fermi energy represented by $E_{\mathrm{gap}} + \Delta E_{\mathrm{BGR}} + \Delta E_{\mathrm{BMS}}$ are marked by green and blue vertical lines, respectively. The carrier concentration obtained from the Seebeck coefficient measurement was used as fixed input parameter for the fitting procedure. In order to obtain modelled line shapes in accordance with the measurements a rigid shift of the spectra due to strain had to be assumed changing the value of E_{gap}. If the strain in the NWs is assumed to be of biaxial type, it ranges from compressive ($\epsilon_{xx} = -5.3 \times 10^{-4}$) for the NW with a carrier concentration of $9.1 \times 10^{18}\,\mathrm{cm}^{-3}$ to tensile ($\epsilon_{xx} = 2.1 \times 10^{-3}$) for the highest doped NW with $n = 5.53 \times 10^{19}\,\mathrm{cm}^{-3}$. While this increase in tensile strain as a function of increasing germanium incorporation is in agreement with the findings of ref. [74] for Ge-doped GaN thin films, its microscopic origin is not clear at the moment.

5.6. Influence of Si-Doping on the Conductivity

In order to compare the results obtained for Ge-doped GaN NWs, which has proven Ge to be a very efficient donor, NWs with different Si-concentrations were analyzed as well. Since the Ga-peak masks the Si-peak, as described in **Chapter 3.2**, the Si-concentration could not be determined by TEM-EDX even for highly Si-doped NWs. Consequently the Si beam equivalent pressure $\mathrm{BEP_{Si}}$ adjusted during growth of the NWs must be used as a measure for the amount of supplied Si.
Single NWs of different doped ensembles were analyzed in the same way as described for Ge-doped NWs above. In **Figure 5.15** the conductivities for individually Si-doped GaN NWs are shown.
While the $\mathrm{BEP_{Si}}$ is increased from 1.5×10^{-11} mbar to 1.25×10^{-9} mbar no systematic change of the conductivity could be observed. The variations of the conductivity within NWs of the same ensemble are as large as the difference for different Si-doped samples. For comparison the values for n.i.d. NWs (determined in **Chapter 5.1.3**) are shown as well. Since the values of all Si-doped NWs varies in the same way as the n.i.d. wires, no significant influence of the increased $\mathrm{BEP_{Si}}$ on the conductivity is observed. A possible explanation could be a dominant contribution of Si-incorporation due to diffusion of Si from the substrate into the NW base, as discussed in **Chapter 5.1.1**, electrically inactive incorporated Si or structural degradation as reported

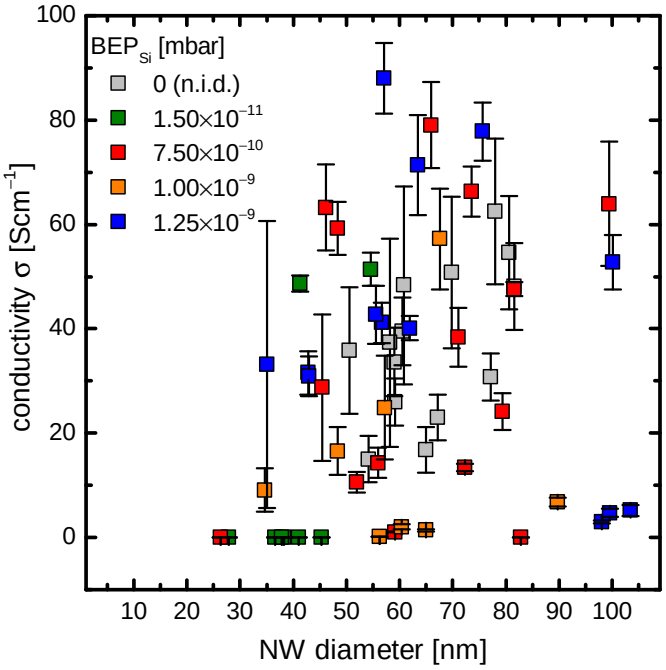

Figure 5.15.: Conductivity of several single NWs doped with silicon as a function of the NW diameter. Values for n.i.d. NWs are shown for comparison.

for NWs with increasing Si-concentration [10, 31, 75], which could cause a lowering of the electron mobility and charge carrier density. Furthermore, even for the ensemble with the highest BEP_{Si} supplied during growth several Si-doped NWs with very high resistances are present, as discussed for the n.i.d. NWs in **Chapter 5.1.1**.
Since the BEP_{Si} are comparable to the BEP_{Ge} used for the growth of Ge-doped NWs, a very ineffective or electrical inactive incorporation of Si in comparison to Ge, or a significant decrease of the mobility or carrier concentration must be present. A further increase of the BEP_{Si} could not be achieved, since the operation temperature of the Knudsen cell used for the effusion of silicon during growth was already at its limits.

Chapter 6

Conclusion

Within this thesis a systematic characterization of the electrical transport properties of single gallium nitride nanowires is presented. For the first time germanium as a shallow donor in gallium nitride nanowires grown by plasma-assisted molecular beam epitaxy is analyzed.

To access electrical measurements on a single nanowire level a state of the art nano-fabrication process was established and continuously improved to achieve high overlay precision and yield. Due to a „mix-and-match“ of two processing technologies the fabrication benefits from fast and parallel processing by photolithography with hard masks for coarse patterns and structuring by electron beam lithography for individual nanosized geometries. The process is very flexible and allows to adopt the geometry depending on the need of the intended measurement. With the final process parameters every NW was matched and the overlay accuracy was improved to less than 10 nm mismatch. Even NWs with a lengths of 1 µm could be contacted with four individual contacts, facilitating electrical measurements in four-point geometry.

For n.i.d. NWs highly resistive NWs with resistances above several MΩ and conductive NWs with a resistance in the range of 40 kΩ to 200 kΩ were observed. The conductivity of the latter can be partially attributed to Si-impurities due to Si-diffusion from the substrate into the NW base, which was determined by spatially resolved conductivity measurements revealing a decreasing conductivity from 81 S/cm to 9 S/cm with increasing distance to the NW base.

A comparative investigation of the resistance measured in two-point and four-point geometry revealed a significant influence of the contact resistances. The latter decreased with increasing germanium concentration and were in the same order of magnitude (10 kΩ) as the resistance of the NW itself evidencing the importance of four-point measurements for single NW characterization.

By elimination of the contact resistances the conductivity was determined taking the NW geometry into account. A continuous increases of the conductivity to an average

of 411 S/cm with increasing [Ge] up to $1.6 \times 10^{20}\,\mathrm{cm}^{-3}$ and a maximum conductivity of 625 S/cm for the sample with the highest [Ge] of $3.3 \times 10^{20}\,\mathrm{cm}^{-3}$ was observed. The conductivity of Ge-doped NWs was independent of the NW diameter whereas for n.i.d. NWs a significant dependence was observed.

The temperature-dependent analysis of the resistance revealed a constant resistance at low temperatures and a small activation energy of 5 meV for temperatures in the range of 80 K to 280 K was observed. The results are attributed to activation from an impurity band formed due to high doping concentrations. Emerging metallic behavior for a NW with a conductivity of 436 S/cm further confirms that Ge is an efficient donor in GaN NWs.

From analysis of the temperature-dependent Seebeck coefficient the charge carrier concentrations could be determined. The values in the range of $9.1 \times 10^{18}\,\mathrm{cm}^{-3}$ to $5.5 \times 10^{19}\,\mathrm{cm}^{-3}$ for a n.i.d. and the highest Ge-doped NW analyzed by this technique were all above the Mott limit and in agreement with the prior results. For these measurements a special sample layout with a meandered micro heater in the vicinity of the NW was used to apply a thermal gradient along the NW.

The carrier mobilities could be estimated by combining both measurement techniques and were almost constant in the range of $10\,\mathrm{cm}^2/\mathrm{Vs}$ to $86\,\mathrm{cm}^2/\mathrm{Vs}$, independent on the carrier concentration.

Photoluminescence spectroscopy of single NWs revealed a clear near band edge emission at 3.485 eV and a slight increase of the FWHM from 35 meV to 70 meV with increasing carrier concentration. In contrast, no significant spectral shift was observable even for the highest doped sample, which could be attributed to a compensation of a blue shift due to band filling effects by a band gap renormalization due to many body effects. In order to obtain modelled line shapes in accordance with the measurements a rigid shift of the spectra due to strain had to be assumed.

Intentional Si-doping showed no significant influence on the transport properties. The variations of the conductivity within NWs of the same ensemble were as large as the difference for different Si-doped samples. The observed conductivities were all below 90 S/cm. In comparison to n.i.d. NWs no significant influence of increased $\mathrm{BEP}_{\mathrm{Si}}$ during growth was observed. Also highly resitive Si-doped NWs were observed. These results can be attributed to ineffective incorporation of Si or electrically inactive Si. The unintentional background doping due to Si-diffusion from the substrate further masks the intended but weak Si-doping.

The presented systematic quantitative analysis of the electrical transport properties determined by different measurement techniques revealed very conclusive results. The results are in good agreement with reports for GaN thin films and n.i.d. and Si-doped

GaN NWs. For the first time germanium has been proven to be a very efficient donor in GaN NWs grown by PAMBE. Germanium doping enables high charge carrier concentrations without structural degradation and should be considered as primary technology for GaN NW based electronics.

Appendix A

Details on Micro- and Nanofabrication

A.1. Transfer of Nanowires

In order to analyze single nanowires they were removed from the substrate and transferred to patterned chips. Due to a temperature gradient on the substrate during growth the degree of coalescence is not homogeneous across the sample. By SEM analysis an area with least coalescence is selected to provide mostly single NWs for the electrical measurements. For this a small piece with an area of 1 mm^2 to 4 mm^2 of a NW ensemble was cleaved, properly cleaned and put into a small glass flask filled with isopropyl alcohol. Then the nanowires were harvested from the Si substrate using an ultrasonic bath. Subsequently the suspended NWs were dispersed on the chip by transfer of several small drops of the suspension using a pipette. After deposition of the NWs the samples were rinsed with isopropyl alcohol and dried in a nitrogen flow.

A.2. Layout Design

The design of the layout was carried out with the CAD software „LayoutEditor“ by juspertor UG[1]. For patterning of the finder grid on the total wafer by a 1st EBL the desired layout was designed straight away. One of the 10 µm × 10 µm sectors of the grid is shown in **Figure A.1 (a)**.
For the fabrication of individual contacts to a single NW by a 2nd EBL a high overlay accuracy had to be achieved. Therefore, a single NW was identified by SEM imaging in one of the sectors of the finder grid, as shown in **Figure A.1 (b)**. The SEM micrograph was superimposed to the layout of the finder grid and consequently the

[1] www.layouteditor.net

desired contacts were drawn as shown in **Figure A.1 (c)**. The final result after EBL, metallization and lift-off is shown in **Figure A.1 (d)**.

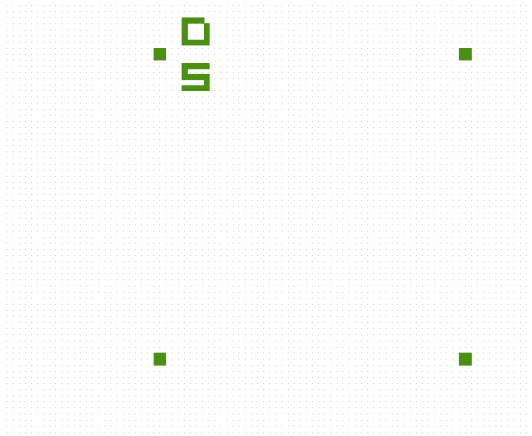

(a) Layout of one sector of the finder grid.

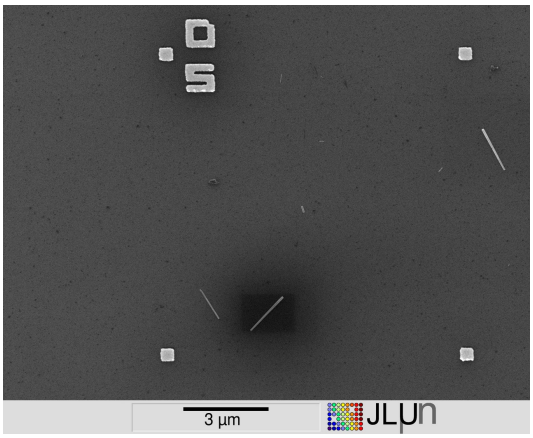

(b) SEM micrograph of single NWs located in sector D5.

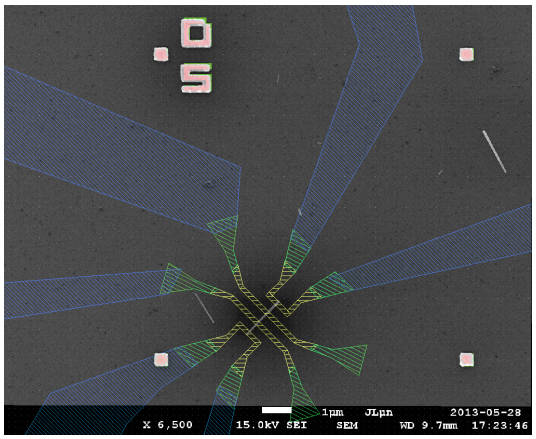

(c) Superimposed layout and SEM micrograph.

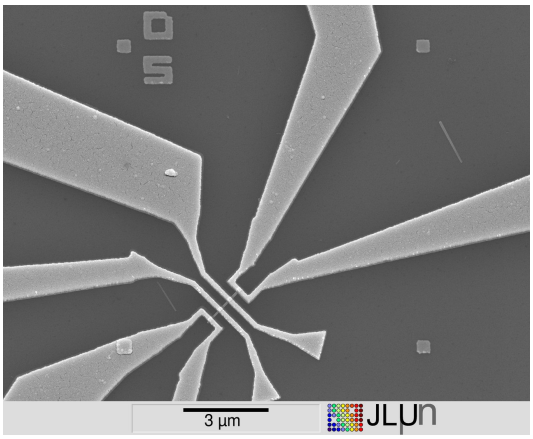

(d) SEM micrograph of the final structure.

Figure A.1.: The layout of one sector of the finder grid is shown in (a). Single NWs localized in sector D5 are shown in (b). Both layout (a) and SEM micrograph (b) are superimposed as shown in (c) and individual contacts to the NW can be designed. The final structure after EBL, metallization and lift-off is shown in (d).

A.3. Details on Aligned EBL

As outlined above, a proper alignment is the key technology to contact single NWs. The alignment is based on a hierarchical detection of several alignment markers. An example for the needed code of a control file for ECP is given in **Listing A.1**.

Listing A.1: Code example for aligned EBL.

```
origin = 0, 0
current = 200
fsize = 200
autorot
gmcoord = 0, 0
gmcoord = 0, 2500
gmcoord = 3000, 2500
gmfile = globalmarkset
gmark(AUTO)
x = 1500
y = 1250
stage
cmcoord = 2500, 8750
cmcoord = 2500, 41250
cmcoord = 47500, 41250
cmcoord = 47500, 8750
cmfile = chipmarkset
cmark
cmark
cmark
sfile = patternfile
draw(criticalpattern, 5, 4000)
draw(normalpattern, 5, 4000)
draw(uncriticalpattern, 5, 4000)
x = 0
y = 0
stage
end
```

In general the sample is rotated in respect to the axis of the stage. Therefore, at the beginning of a lithography the rotation is compensated by the procedure *autorot*. To use *autorot* two reference points on the sample that are on a vertical or horizontal line must be defined. The rotation of the sample is calculated with a trigonometrical function. Consequently the coordinates of the globalmarks (in µm) defined in the ECP coordinate system are corrected to match the sample coordinate system prior to the detection of the globalmarks. If the JEOL SEM sample holder is used one should rather adjust a rotation of the sample by rotating the stage before the exposure is started than making use of *autorot*. For the usage of the XENOS XeMove stage, which provides no possibility of rotation, the automatic correction is beneficial, often essential.

Each chip processed by photolithography has three large crosses called globalmarks located at the corners and a set of eight small crosses called chipmarks in the center of the chip. SEM micrographs are given in **Figure A.2**, in **(a)** a complete chip is shown and the globalmarks are marked by circles (compare scheme in **Figure 4.1**). In **Figure A.2 (b)** a magnified view of the EBL writing field with eight chipmarks at the center of the chip is presented. At the beginning of the EBL the lower left cross of the globalmarks has to be searched manually and set as origin. All three globalmarks are used to properly map the coordinate system of the sample on the stage to the coordinate system of ECP using the *gmark* function. After that a precise movement to the center of the chip where the chipmarks are located is ensured.

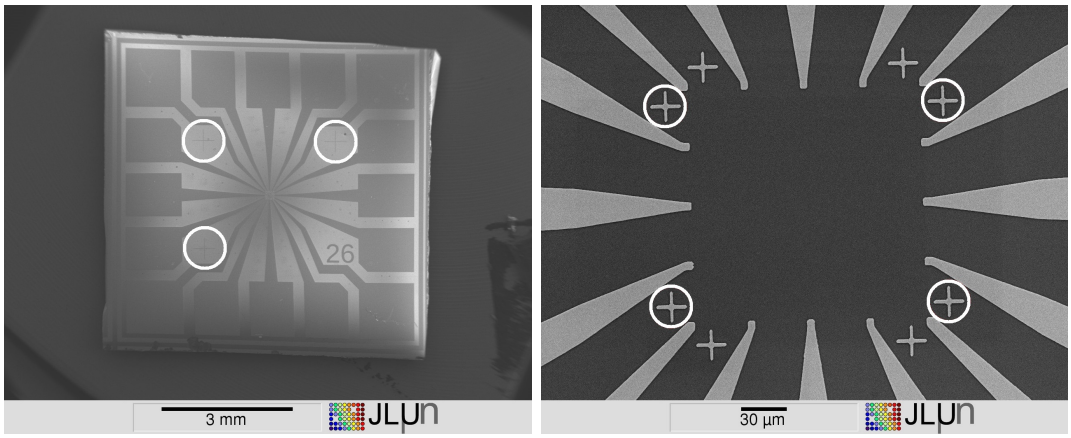

(a) Single Chip. (b) Centered EBL writing field.

Figure A.2.: SEM micrographs of (a) a single chip with three globalmarks and (b) the centered writing field for EBL (200 µm x 200 µm) with eight chipmarks. The used marks are marked by circles.

After complete detection of the globalmarks and movement to the center of the chip the chipmarks (coordinates defined in pixel) are detected without any movement of the stage as they are all located inside the 200 µm x 200 µm (corresponds to 50000 pixel x 50000 pixel) EBL writing field. The electron beam is deflected to the defined areas to detect the marks without exposure of the rest of the field. The defined coordinates of the chipmarks and the real detected ones are compared and the deviation is used to transform the coordinate system in order to realize a high overlay accuracy of the defined strucutres in respect to the sample. To improve the accuracy the detection of the chipmarks is repeated several times.

Thermal Drift:

Since the sample moves due to thermal drift it is an important step to write critical patterns that have to match the NW directly after the detection of the chipmarks. These structures have a small area and only a short writing time. Consequently larger patterns which need more writing time and are less important for optimum overlay accuracy should be written later. It is essential to design patterns with a certain overlap to compensate the drift. In **Figure A.3 (a)** a small drift with respect to the layout in **Figure A.3 (b)** is visible but was compensated due to sufficient overlap in the design. Only on very rare occasions the drift was so pronounced that short circuits or open circuits occurred as shown in **Figure A.4**.

Systematic error:

Even for ideal conditions a systematic misalignment was present. The average shift over several samples, all written after detection of the chipmarks with the same

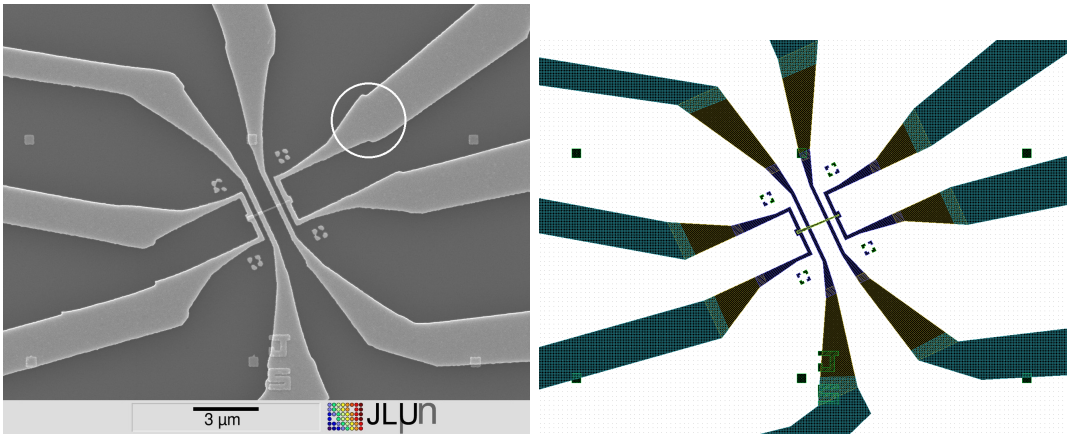

(a) SEM micrograph. (b) Designed layout.

Figure A.3.: Illustration of the influence of the thermal drift. (a) SEM micrograph and (b) designed layout do not perfectly match for the later written structures due to a small thermal drift. To guide the eye one spot is marked with a circle.

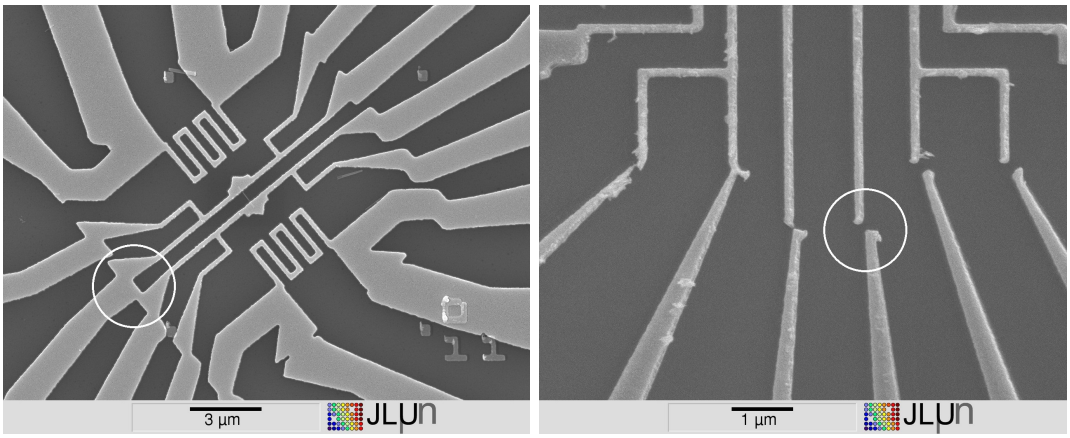

(a) Short circuit. (b) Open circuit.

Figure A.4.: On rare occasions the thermal drift was so pronounced that (a) short circuits or (b) open circuits occured. To guide the eye exemplarily spots are marked with a circle.

parameter set, were determined[2] to approximately x = 50 nm and y = 100 nm. If the pattern was moved by the same amount in the CAD layout beforehand, the final result matches almost perfectly with the NW. **Figure A.5 (a)** shows the intentionally shifted layout and **(b)** the resulting high overlay accuracy to the NW with less than 10 nm shift.

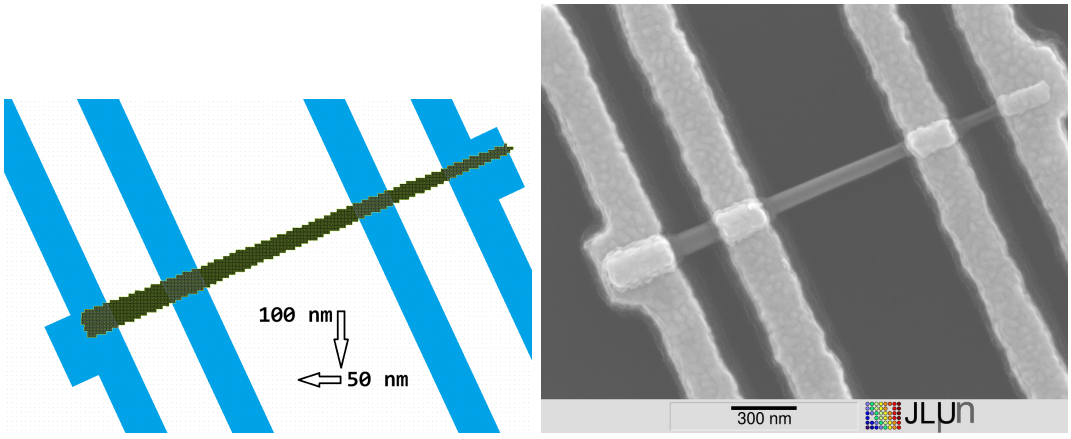

(a) Layout. (b) SEM micrograph.

Figure A.5.: To compensate the systematic shift the layout of the designed contacts (a) was intentionally translated by x = 50 nm and y = 100 nm with respect to the NW. Consequently the overlay accuracy between metal contacts and NW (b) is better than 10 nm.

The strategy of writing critical structures directly after the alignment additionally enables very fast processing. No waiting time for thermalization of sample, holder and stage is needed. A sample set consisting of four chips can be processed in less than one hour including the time for loading and unloading.

A.4. Proximity Effect

A common problem in EBL is the proximity effect. As the electrons penetrate through the resist into the substrate, they occasionally undergo large angle scattering and back scattered electrons increase the effective dose of a feature nearby the intentionally exposed area. Consequently, the dose delivered by the electron beam tool is not confined to the writing areas resulting in pattern-specific line width variations known as the proximity effect. Since the exposure control program (ECP) of the XENOS EBL system has no computational proximity correction[3] the correction must be carried

[2] The amount of the systematic error depends on the parameters forthe mark detection. If parameters are changed, for example the dwell time, it will influence the systematic shift.

[3] SCELETON™ or PROXECCO™ by Synopsys are suited software packages for calculation of the right dose depending on the shape of a structure. E.g. to write a rectangle the dose will be

out either by manual dose adjustments for specific parts of the pattern or by layout modification in the CAD file. The impact of the proximity effect depends on the substrate [76], acceleration voltage, resist material and thickness.

A.5. Dose Optimization and Calculation

To transfer the target structures from the layout to the sample the right dose D defined as charge per area for the exposure should be determined by a dose test. The dose roughly scales with the acceleration voltage and for the used EBL setup with 15 keV electrons a dose of 200 µC/cm^2 was determined to be optimum. The dose can be changed by the beam current I, the dwell time t_{dwell} which determines how long an area A_{expo} is exposed and by A_{expo} itself. Depending on the length of the field size L_{field} it might happen that the dwell time has to be smaller than 100 ns to match the right dose. Since 100 ns is the lower limit for the 10 MHz pattern generator one has to consolidate a certain amount N of pixels with the length L_{pix} in both directions and expose those together accordingly for a longer time. The parameter determining how many pixels are consolidated is called increment N. The electron beam is moved in pixels and L_{field} corresponds to 50000 pixels. Depending on these parameters[4] the dose can be calculated according to equation A.1.

$$D = \frac{I \times t_{\mathsf{dwell}}}{A_{\mathsf{expo}}} = \frac{I \times t_{\mathsf{dwell}}}{(N \times L_{\mathsf{pix}})^2} = \frac{I \times t_{\mathsf{dwell}}}{(N \times \frac{L_{\mathsf{field}}}{50000})^2} = \frac{I \times t_{\mathsf{dwell}} \times 25 \times 10^8}{N^2 \times L_{\mathsf{field}}^2} \qquad \text{(A.1)}$$

In general the best resolution is achieved for small current, increment and dwell time but additionally the limited operation frequency of the EBL system also has to be be taken into account. Very good parameters for a field size length of 200 µm and a beam current of 200 pA were increment 5 and dwell time 4000 ns. With the latter parameters, compared to increment 1 and a dwell time of 160 ns, the actual operation frequency of the pattern generator is decreased to 250 kHz compared to 6.25 MHz which leads to more reliable operation.

A.6. Focus

For the precise reproduction of structures the adjustment of the electron beam focus is of essential importance. Due to parasitic exposure during manual focusing it is not

increased at the sides and especially at the corners in comparison to the internal of the pattern.

[4] In Xenos syntax for the description of a pattern file, the parameters have different names: $I = N$ (increment), $C = t_{\mathsf{dwell}}$ (dwell time), $FSIZE = L_{\mathsf{field}}$ (field size)

possible to focus inside the writing field. Consequently two different approaches can be pursued.
The first approach is called „working distance correction“ and uses the command *setfocus(*)* of ECP. The focus is manually set at three spots surrounding the target writing area and the corresponding z values are submitted to ECP. With the coordinates of these three points ECP calculates a plane across the sample. Consequently, ECP automatically sets the focus for every writing field depending on the actual x and y coordinates during the exposure. This approach gives good results and is suitable if many fields are written. Occasionally the sample is bowed by the clamp fixing it to the sample holder. In that case this approach will not lead to good results.

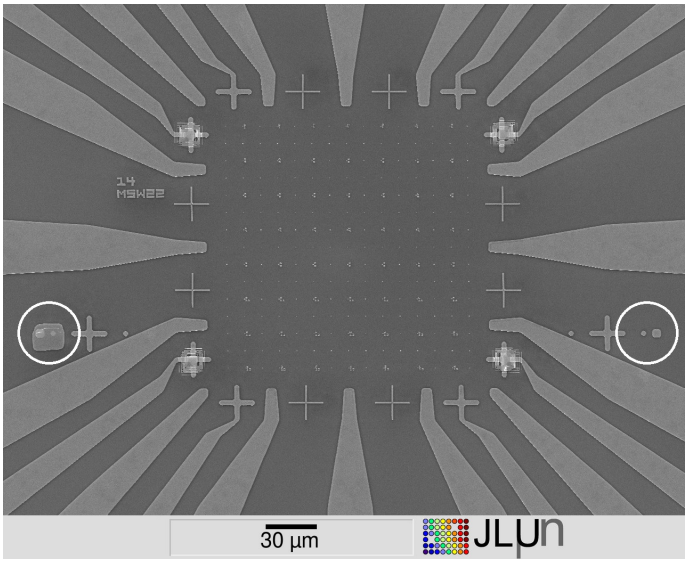

Figure A.6.: SEM micrograph of the center of a chip with the finder grid already pattered by the first EBL. The parasitic exposure due to manual focusing is marked with a circle on the left. In comparison on the right the unexposed structure is marked. It can be used for the second EBL.

The second approach is based on manually focusing in the immediate vicinity of every single writing field. For the samples processed in this thesis this approach was practicable as on each chip only one field in the center was written. For this purpose a modified mask for photolithography with small structures useable for focusing very close to the writing field was designed. **Figure A.6** illustrates the parasitic exposure of the marker used for focusing in comparison to the unexposed marker that could be used for the second EBL. With this method the best results were obtained.
To implement the second approach to the workflow the code snippet given in **Listing A.2** should be inserted between line 9 and 10 of the code example given in **Listing A.1**. The command *fsize* changes the magnification of the SEM to a higher value to reduce the parasitic exposed area when the beam is not blanked. Since the

code follows the detection of the globalmarks the stage can be moved exactly to the location of the focus mark and parasitic exposure is minimized. The followed command *pause* allows to cancel the exposure and the operator can manually set the focus. Then the exposure is started again from the beginning and can be continued as the command *pause* is reached again.

Listing A.2: Code snippet for semi manual focusing. It has to be inserted between line 9 and 10 of the code example given in **Listing A.1**

```
1 fsize = 10
2 x = 1330
3 y = 1202
4 stage
5 pause
6 fsize = 200
```

To illustrate the importance of focusing a structure written with wrong focus[5] is shown in **Figure A.7 (a)**. In contrast, a structure that was written when the focus was set well in the vicinity to the writing field is shown in **Figure A.7 (b)**.

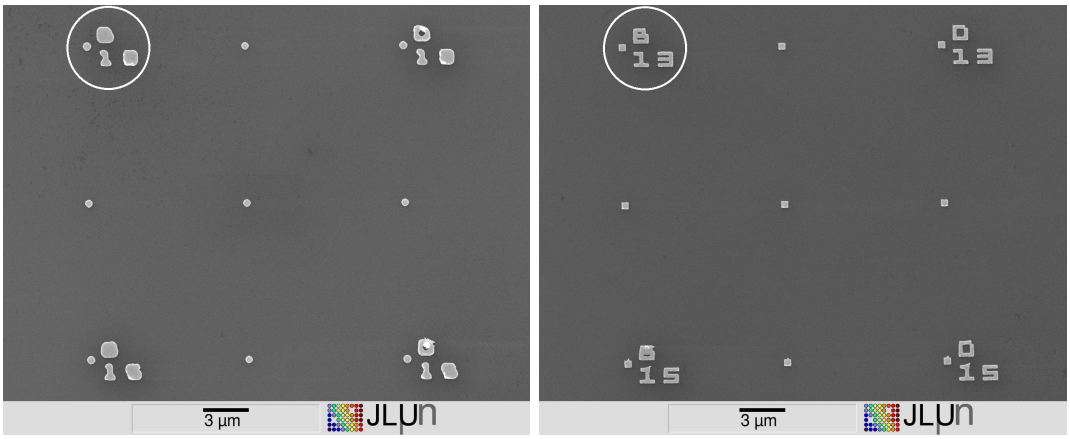

(a) Bad focus. (b) Good focus.

Figure A.7.: SEM micrograph of (a) a chip written with focus set wrong and (b) focused well in the vicinity to the centered writing field. In (a) small features could not be transferred and squares became circles in comparison to precise transferred structures in (b).

A.7. Lift-off Process

The process described in the following, known as lift-off, was reported in 1969 by Hatzakis *et al.* [77] for Poly(methyl methacrylate) (PMMA) as one of the first materials for e-beam lithography. Today PMMA is still the standard positive e-beam resist,

[5] The focus was set at another chip 7 mm away.

since it remains as one of the highest resolution but soluble and light insensitive resists available. During exposure the high energy electrons of the beam cracks the polymer into fragments that are afterwards preferentially dissolved by a developer such as a 2:1 mixture of isopropyl alcohol (IPA) and water (H_2O). When exposed to more than the tenfold of the optimal dose, PMMA will cross-link, forming a negative resist. This effect can be easily observed after focusing or scanning on a mark for an extended time. The center of the spot will be cross-linked, leaving resist on the substrate, while the surrounding area is exposed positively and is washed away by the developer.
After development in the resist a undercut profile is present, as shown in the scheme in the inset of **Figure A.8 (a)**. Due to this undercut profile a discontinuity between metal in the developed gap and on top of the resist remains after metallization. This gap allows the solvent to access the unexposed PMMA and remove it together with the metal layer on to of it.

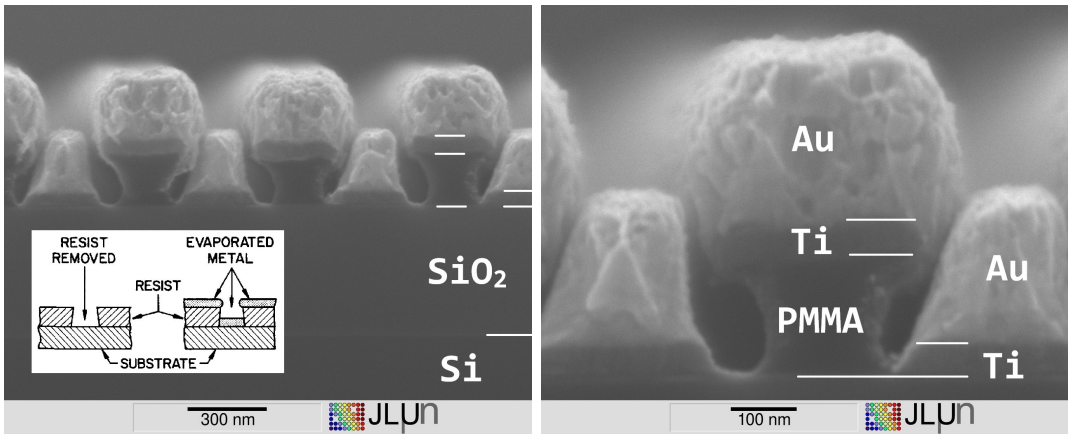

(a) Cross section and undercut profile. (b) Magnified cross section.

Figure A.8.: Cross section of a cleaved sample. Different layers can clearly be distinguished. The inset in (a) shows a scheme of the undercut profile. Scheme taken from ref. [77].

In this thesis the positive resists PMMA with a molecular weight of 950 K, 4% solids dissolved in anisol, was used for EBL. The thickness was adjusted from 200 nm to 400 nm by choosing different rotational speeds from 4000 rpm to 2000 rpm (revolutions per minute) for spin coating depending on whether high resolution or thick metal layers should be realized.
A scheme of the undercut profile and a cross-section of a cleaved sample after metallization is shown in **Figure A.8**. The undercut in the PMMA can be identified by the T-shaped structure. The interface between silicon and silicon dioxide can be seen, with a oxide thickness of 490 nm. Also the titanium layer can clearly be distinguished between substrate and gold layer. The thickness of the complete metal layer differs in

the gap and on top of the PMMA. The film has a thickness of 287 nm (Ti 53 nm, Au 234 nm) on the silicon oxide in the gap and 335 nm (Ti 60 nm, Au 275 nm) on top of the PMMA, which can be attributed to a shadowing effect. The determination of the thickness of the PMMA layer is difficult by SEM due to a deformation of the PMMA by electron beam exposure. The deformation is shown before and after electron beam exposure in **Figure A.9 (a)** and **(b)**, respectively. The thickness of the PMMA layer decreases from 300 nm to 182 nm and a clear bowing of the metal layer is visible. To verify the PMMA layer thickness samples were processed with exactly the same parameters and analyzed by atomic force microscopy. One sample was measured after development and the second after metallization and lift-off. The thickness of the layers could be determined to (300 ± 10) nm and (265 ± 10) nm for PMMA and metal film, respectively. These values are comparable to the results obtained by SEM analysis. The error of ± 10 nm is correlated to local variations of the thickness.

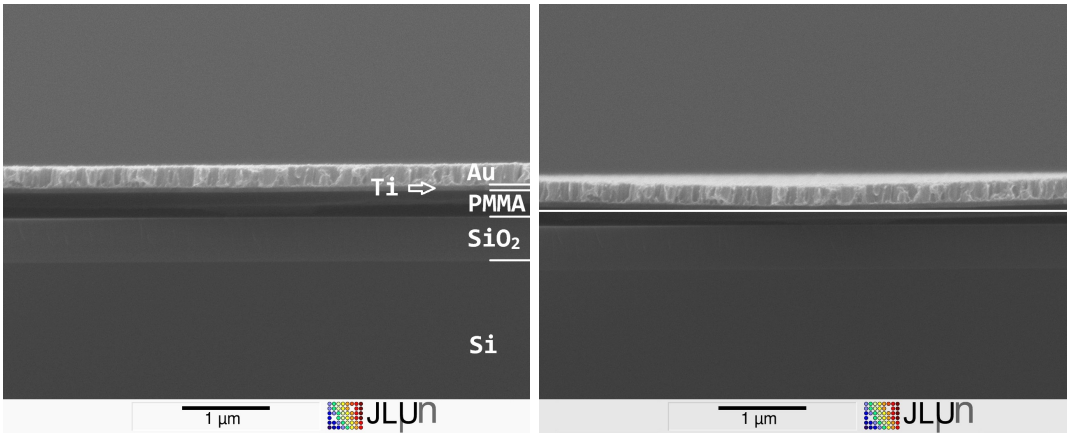

(a) Cross section before... (b) ..and after extended e-beam exposure.

Figure A.9.: Cross section of a cleaved sample. A deformation of the PMMA can be observed due to e-beam exposure. The deformation leads to a bowing of the metal layer. The white line at the interface between PMMA and metal guides the eye to notice the bowing.

The maximum thickness of deposited metal is limited by the undercut profile depending on the PMMA layer thickness. If the metal layer is too thick and the gap is covered no solvent can reach the resist and no lift-off is possible. In general a thicker layer of resists allows a thicker metal layer. On the other hand the resolution of EBL is decreased with increasing resist thickness. Therefore, a minimum resist thickness has to be determined to realize high resolution structures. In this work the diameter of the nanowires determined the needed thickness of the metal layer. To obtain complete wrapping and good electrical contacts the metal layer thickness was chosen to be approximately twice the NW diameter.

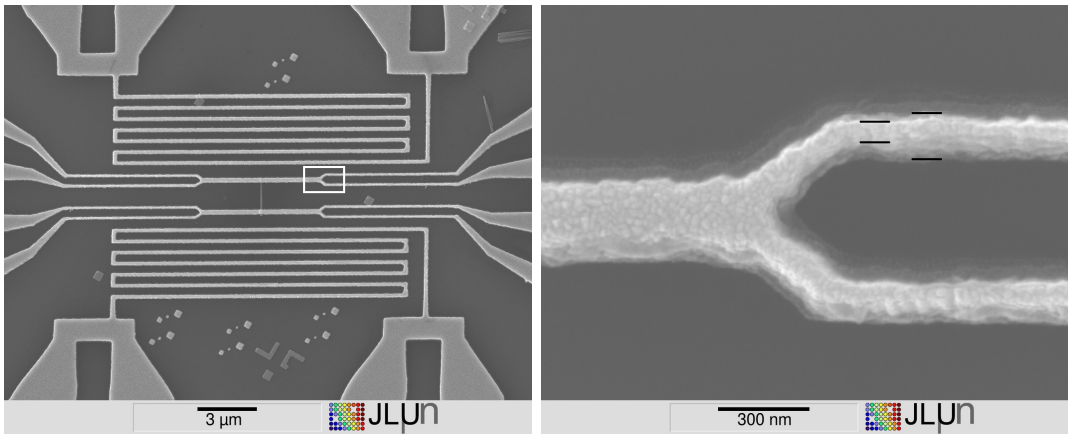

(a) SEM micrograph. (b) Magnified view.

Figure A.10.: SEM micrograph of a sample (a) with high aspect ratio structures. The thinnest lines shown on the right of the magnified view in (b) have a aspect ratio of 3, since the width of the line is (85 ± 15) nm and the metal layer has a thickness of 290 nm.

The line width of the structure shown in **Figure A.8** is approximately 120 nm on the top and 250 nm on the bottom, since the thickness of the metal is approximately 290 nm the structure has a aspect ratio larger than one. A sample with thinner lines and a metal layer with the same thickness is shown in **Figure A.10**. In that case the line has a width of (70 ± 5) nm on the top and (100 ± 5) nm on the bottom and the aspect ratio is in the order of 3. For all prepared samples in this thesis only single resist layer technology was used.

Bibliography

[1] I. Tuomi, *The Lives and Death of Moore's Law*, First Monday **7** (2002), DOI: 10.5210/fm.v7i11.1000.

[2] W. Arden, M. Brillouët, P. Cogez, M. Graef, B. Huizing, and R. Mahnkopf, *"More-than-Moore" White Paper* (2010), `http://www.itrs.net/Links/2010ITRS/IRC-ITRS-MtM-v2%203.pdf`.

[3] X. Chen, C. K. Y. Wong, C. A. Yuan, and G. Zhang, *Nanowire-based gas sensors*, Sensor. Actuat. B-Chem. **177** (2013), 178–195, DOI: 10.1016/j.snb.2012.10.134.

[4] O. Ambacher, *Growth and Applications of Group III-Nitrides*, J. Phys. D: Appl. Phys. **31** (1998), 2653–2710, DOI: 10.1088/0022-3727/31/20/001.

[5] V. Davydov, A. Klochikhin, V. Emtsev, D. Kurdyukov, S. Ivanov, V. Vekshin, F. Bechstedt, J. Furthmüller, J. Aderhold, J. Graul, A. Mudryi, H. Harima, A. Hashimoto, A. Yamamoto, and E. Haller, *Band Gap of Hexagonal InN and InGaN Alloys*, physica status solidi (b) **234** (2002), 787–795, DOI: 10.1002/1521-3951(200212)234:3<787::AID-PSSB787>3.0.CO;2-H.

[6] J. P. Ibbetson, P. T. Fini, K. D. Ness, S. P. DenBaars, J. S. Speck, and U. K. Mishra, *Polarization effects, surface states, and the source of electrons in AlGaN/-GaN heterostructure field effect transistors*, Appl. Phys. Lett. **77** (2000), 250–252, DOI: 10.1063/1.126940.

[7] S. W. Kaun, M. H. Wong, U. K. Mishra, and J. S. Speck, *Molecular beam epitaxy for high-performance Ga-face GaN electron devices*, Semicond. Sci. Technol. **28** (2013), 074001, DOI: 10.1088/0268-1242/28/7/074001.

[8] F. Glas, *Critical dimensions for the plastic relaxation of strained axial heterostructures in free-standing nanowires*, Phys. Rev. B **74** (2006), 121302, DOI: 10.1103/PhysRevB.74.121302.

[9] F. Furtmayr, M. Vielemeyer, M. Stutzmann, J. Arbiol, S. Estradé, F. Peirò, J. R. Morante, and M. Eickhoff, *Nucleation and growth of GaN nanorods on Si (111) surfaces by plasma-assisted molecular beam epitaxy - The influence of Si- and Mg-doping*, J. Appl. Phys. **104** (2008), 034309, DOI: 10.1063/1.2953087.

[10] J. Schörmann, P. Hille, M. Schäfer, J. Müßener, P. Becker, P. J. Klar, M. Kleine-Boymann, M. Rohnke, M. de la Mata, J. Arbiol, D. M. Hofmann, J. Teubert, and M. Eickhoff, *Germanium doping of self-assembled GaN nanowires grown by plasma-assisted molecular beam epitaxy*, J. Appl. Phys. **114** (2013), 103505, DOI: 10.1063/1.4820264.

[11] F. Schuster, F. Furtmayr, R. Zamani, C. Magén, J. R. Morante, J. Arbiol, J. A. Garrido, and M. Stutzmann, *Self-Assembled GaN Nanowires on Diamond*, Nano Lett. **12** (2012), 2199–2204, DOI: 10.1021/nl203872q.

[12] C. Chèze, L. Geelhaar, O. Brandt, W. M. Weber, H. Riechert, S. Münch, R. Rothemund, S. Reitzenstein, A. Forchel, T. Kehagias, P. Komninou, G. P. Dimitrakopulos, and T. Karakostas, *Direct comparison of catalyst-free and catalyst-induced GaN nanowires*, Nano Research **3** (2010), 528–536, DOI: 10.1007/s12274-010-0013-9.

[13] Y. Li, F. Qian, J. Xiang, and C. M. Lieber, *Nanowire electronic and optoelectronic devices*, Materials Today **9** (2006), 18–27, DOI: 10.1016/S1369-7021(06)71650-9.

[14] S. Li and A. Waag, *GaN based nanorods for solid state lighting*, J. Appl. Phys. **111** (2012), 071101, DOI: 10.1063/1.3694674.

[15] R. S. Chen, C. Y. Lu, K. H. Chen, and L. C. Chen, *Molecule-modulated photoconductivity and gain-amplified selective gas sensing in polar GaN nanowires*, Appl. Phys. Lett. **95** (2009), 233119, DOI: 10.1063/1.3264954.

[16] C. P. Chen, A. Ganguly, C. H. Wang, C. W. Hsu, S. Chattopadhyay, Y. K. Hsu, Y. C. Chang, K. H. Chen, and L. C. Chen, *Label-Free Dual Sensing of DNA Molecules Using GaN Nanowires*, Anal. Chem. **81** (2009), 36–42, DOI: 10.1021/ac800986q.

[17] J. Teubert, P. Becker, F. Furtmayr, and M. Eickhoff, *GaN nanodiscs embedded in nanowires as optochemical transducers*, Nanotechnology **22** (2011), 275505, DOI: 10.1088/0957-4484/22/27/275505.

[18] C.-P. Chen, A. Ganguly, C.-Y. Lu, T.-Y. Chen, C.-C. Kuo, R.-S. Chen, W.-H. Tu, W. B. Fischer, K.-H. Chen, and L.-C. Chen, *Ultrasensitive in Situ Label-Free DNA Detection Using a GaN Nanowire-Based Extended-Gate Field-Effect-Transistor Sensor*, Anal. Chem. **83** (2011), 1938–1943, DOI: 10.1021/ac102489y.

[19] R. Bajpai, A. Motayed, A. V. Davydov, V. P. Oleshko, G. S. Aluri, K. A. Bertness, M. V. Rao, and M. E. Zaghloul, *UV-assisted alcohol sensing using SnO_2 functionalized GaN nanowire devices*, Sensor. Actuat. B-Chem. **171–172** (2012), 499–507, DOI: 10.1016/j.snb.2012.05.018.

[20] G. S. Aluri, A. Motayed, A. V. Davydov, V. P. Oleshko, K. A. Bertness, N. A. Sanford, and R. V. Mulpuri, *Methanol, ethanol and hydrogen sensing using metal oxide and metal (TiO_2-Pt) composite nanoclusters on GaN nanowires: a new route towards tailoring the selectivity of nanowire/nanocluster chemical sensors*, Nanotechnology **23** (2012), 175501, DOI: 10.1088/0957-4484/23/17/175501.

[21] J. Wallys, J. Teubert, F. Furtmayr, D. M. Hofmann, and M. Eickhoff, *Bias-Enhanced Optical pH Response of Group III-Nitride Nanowires*, Nano Lett. **12** (2012), 6180–6186, DOI: 10.1021/nl303021v.

[22] S. Paul, A. Helwig, G. Müller, F. Furtmayr, J. Teubert, and M. Eickhoff, *Opto-chemical sensor system for the detection of H_2 and hydrocarbons based on InGaN/GaN nanowires*, Sensor. Actuat. B-Chem. **173** (2012), 120–126, DOI: 10.1016/j.snb.2012.06.022.

[23] K. Maier, A. Helwig, G. Müller, P. Becker, P. Hille, J. Schörmann, J. Teubert, and M. Eickhoff, *Detection of oxidising gases using an optochemical sensor system based on GaN/InGaN nanowires*, Sensor. Actuat. B-Chem. **197** (2014), 87–94, DOI: 10.1016/j.snb.2014.02.002.

[24] M. D. Brubaker, P. T. Blanchard, J. B. Schlager, A. W. Sanders, A. Roshko, S. M. Duff, J. M. Gray, V. M. Bright, N. A. Sanford, and K. A. Bertness, *On-Chip Optical Interconnects Made with Gallium Nitride Nanowires*, Nano Lett. **13** (2013), 374–377, DOI: 10.1021/nl303510h.

[25] Y. Huang, X. Duan, Y. Cui, and C. M. Lieber, *Gallium Nitride Nanowire Nanodevices*, Nano Lett. **2** (2002), 101–104, DOI: 10.1021/nl015667d.

[26] P. Blanchard, K. Bertness, T. Harvey, A. Sanders, N. Sanford, S. M. George, and D. Seghete, *MOSFETs Made From GaN Nanowires With Fully Conformal Cylindrical Gates*, Nanotechnology, IEEE Transactions on **11** (2012), 479–482, DOI: 10.1109/T-NANO.2011.2177993.

[27] F. Furtmayr, J. Teubert, P. Becker, S. Conesa-Boj, J. R. Morante, A. Chernikov, S. Schäfer, S. Chatterjee, J. Arbiol, and M. Eickhoff, *Carrier confinement in GaN/$Al_xGa_{1-x}N$ nanowire heterostructures ($0 < x \leq 1$)*, Phys. Rev. B **84** (2011), 205303, DOI: 10.1103/PhysRevB.84.205303.

[28] J. Arbiol, M. de la Mata, M. Eickhoff, and A. F. i Morral, *Bandgap engineering in a nanowire: self-assembled 0, 1 and 2D quantum structures*, Materials Today **16** (2013), 213–219, DOI: 10.1016/j.mattod.2013.06.006.

[29] T. Kehagias, G. P. Dimitrakopulos, P. Becker, J. Kioseoglou, F. Furtmayr, T. Koukoula, I. Häusler, A. Chernikov, S. Chatterjee, T. Karakostas, H.-M. Solowan, U. T. Schwarz, M. Eickhoff, and P. Komninou, *Nanostructure and strain in InGaN/GaN superlattices grown in GaN nanowires*, Nanotechnology **24** (2013), 435702, DOI: 10.1088/0957-4484/24/43/435702.

[30] M. Beeler, P. Hille, J. Schörmann, J. Teubert, M. de la Mata, J. Arbiol, M. Eickhoff, and E. Monroy, *Intraband Absorption in Self-Assembled Ge-Doped GaN/AlN Nanowire Heterostructures*, Nano Lett. **14** (2014), 1665–1673, DOI: 10.1021/nl5002247.

[31] T. Richter, H. Lüth, R. Meijers, R. Calarco, and M. Marso, *Doping Concentration of GaN Nanowires Determined by Opto-Electrical Measurements*, Nano Lett. **8** (2008), 3056–3059, DOI: 10.1021/nl8014395.

[32] L. Mansfield, K. Bertness, P. Blanchard, T. Harvey, A. Sanders, and N. Sanford, *GaN Nanowire Carrier Concentration Calculated from Light and Dark Resistance Measurements*, J. Electron. Mater. **38** (2009), 495–504, DOI: 10.1007/s11664-009-0672-z.

[33] N. A. Sanford, P. T. Blanchard, K. A. Bertness, L. Mansfield, J. B. Schlager, A. W. Sanders, A. Roshko, B. B. Burton, and S. M. George, *Steady-state and transient photoconductivity in c-axis GaN nanowires grown by nitrogen-plasma-assisted molecular beam epitaxy*, J. Appl. Phys. **107** (2010), 034318, DOI: 10.1063/1.3275888.

[34] N. A. Sanford, L. H. Robins, P. T. Blanchard, K. Soria, B. Klein, B. S. Eller, K. A. Bertness, J. B. Schlager, and A. W. Sanders, *Studies of photoconductivity and field effect transistor behavior in examining drift mobility, surface depletion, and transient effects in Si-doped GaN nanowires in vacuum and air*, J. Appl. Phys. **113** (2013), 174306, DOI: 10.1063/1.4802689.

[35] P. Tchoulfian, F. Donatini, F. Levy, B. Amstatt, P. Ferret, and J. Pernot, *High conductivity in Si-doped GaN wires*, Appl. Phys. Lett. **102** (2013), 122116, DOI: 10.1063/1.4799167.

[36] P. Tchoulfian, F. Donatini, F. Levy, B. Amstatt, A. Dussaigne, P. Ferret, E. Bustarret, and J. Pernot, *Thermoelectric and micro-Raman measurements of carrier density and mobility in heavily Si-doped GaN wires*, Appl. Phys. Lett. **103** (2013), 202101, DOI: 10.1063/1.4829857.

[37] H. Wang and A.-B. Chen, *Calculation of shallow donor levels in GaN*, J. Appl. Phys. **87** (2000), 7859–7863, DOI: 10.1063/1.373467.

[38] W. Götz, R. S. Kern, C. H. Chen, H. Liu, D. A. Steigerwald, and R. M. Fletcher, *Hall-effect characterization of III-V nitride semiconductors for high efficiency light emitting diodes*, Mater. Sci. Eng. B-Adv. **59** (1999), 211–217, DOI: 10.1016/S0921-5107(98)00393-6.

[39] M. Kumar, T. N. Bhat, B. Roul, M. K. Rajpalke, A. Kalghatgi, and S. Krupanidhi, *Carrier concentration dependence of donor activation energy in n-type GaN epilayers grown on Si(111) by plasma-assisted MBE*, Mater. Res. Bull. **47** (2012), 1306–1309, DOI: 10.1016/j.materresbull.2012.03.016.

[40] J. Jayapalan, B. J. Skromme, R. P. Vaudo, and V. M. Phanse, *Optical spectroscopy of Si-related donor and acceptor levels in Si-doped GaN grown by hydride vapor phase epitaxy*, Appl. Phys. Lett. **73** (1998), 1188–1190, DOI: 10.1063/1.122123.

[41] P. Bogusławski and J. Bernholc, *Doping properties of C, Si, and Ge impurities in GaN and AlN*, Phys. Rev. B **56** (1997), 9496–9505, DOI: 10.1103/PhysRevB.56.9496.

[42] P. Hageman, W. Schaff, J. Janinski, and Z. Liliental-Weber, *n-type doping of wurtzite GaN with germanium grown with plasma-assisted molecular beam epitaxy*, J. Cryst. Growth **267** (2004), 123–128, DOI: 10.1016/j.jcrysgro.2004.03.024.

[43] P. Hille, J. Müßener, P. Becker, M. de la Mata, N. Rosemann, C. Magén, J. Arbiol, J. Teubert, S. Chatterjee, J. Schörmann, and M. Eickhoff, *Screening of the quantum-confined Stark effect in AlN/GaN nanowire superlattices by germanium doping*, Appl. Phys. Lett. **104** (2014), 102104, DOI: 10.1063/1.4868411.

[44] C. Blömers, T. Grap, M. I. Lepsa, J. Moers, S. Trellenkamp, D. Grützmacher, H. Lüth, and T. Schäpers, *Hall effect measurements on InAs nanowires*, Appl. Phys. Lett. **101** (2012), 152106, DOI: 10.1063/1.4759124.

[45] K. Storm, F. Halvardsson, M. Heurlin, D. Lindgren, A. Gustafsson, P. M. Wu, B. Monemar, and L. Samuelson, *Spatially resolved Hall effect measurement in a single semiconductor nanowire*, Nature Nanotechnology **7** (2012), 718–722, DOI: 10.1038/nnano.2012.190.

[46] J. P. DeGrave, D. Liang, and S. Jin, *A General Method To Measure the Hall Effect in Nanowires: Examples of FeS_2 and MnSi*, Nano Lett. **13** (2013), 2704–2709, DOI: 10.1021/nl400875z.

[47] C. Fernandes, H. E. Ruda, and A. Shik, *Hall effect in nanowires*, J. Appl. Phys. **115** (2014), 234304, DOI: 10.1063/1.4884681.

[48] H.-Y. Cha, H. Wu, M. Chandrashekhar, Y. C. Choi, S. Chae, G. Koley, and M. G. Spencer, *Fabrication and characterization of pre-aligned gallium nitride nanowire field-effect transistors*, Nanotechnology **17** (2006), 1264, DOI: 10.1088/0957-4484/17/5/018.

[49] E. Stern, G. Cheng, E. Cimpoiasu, R. Klie, S. Guthrie, J. Klemic, I. Kretzschmar, E. Steinlauf, D. Turner-Evans, E. Broomfield, J. Hyland, R. Koudelka, T. Boone, M. Young, A. Sanders, R. Munden, T. Lee, D. Routenberg, and M. A. Reed, *Electrical characterization of single GaN nanowires*, Nanotechnology **16** (2005), 2941, DOI: 10.1088/0957-4484/16/12/037.

[50] M.-H. Ham, J.-H. Choi, W. Hwang, C. Park, W.-Y. Lee, and J.-M. Myoung, *Contact characteristics in GaN nanowire devices*, Nanotechnology **17** (2006), 2203, DOI: 10.1088/0957-4484/17/9/021.

[51] H. B. Huo, C. Liu, L. Dai, L. P. You, W. Q. Yang, R. M. Ma, Y. F. Zhang, and G. G. Qin, *A method to identify shallow dopants in semiconductor nanowires*, Appl. Phys. Lett. **91** (2007), 181117, DOI: 10.1063/1.2805019.

[52] K. Storm, G. Nylund, L. Samuelson, and A. P. Micolich, *Realizing Lateral Wrap-Gated Nanowire FETs: Controlling Gate Length with Chemistry Rather than Lithography*, Nano Lett. **12** (2012), 1–6, DOI: 10.1021/nl104403g.

[53] C.-H. Lee, G.-C. Yi, Y. M. Zuev, and P. Kim, *Thermoelectric power measurements of wide band gap semiconducting nanowires*, Appl. Phys. Lett. **94** (2009), 022106, DOI: 10.1063/1.3067868.

[54] P. Hille, *Wachstum und Charakterisierung komplexer Gruppe III-Nitrid Nanostrukturen*, Masterarbeit, Justus-Liebig-Universität Gießen (2012).

[55] R. Calarco, T. Stoica, O. Brandt, and L. Geelhaar, *Surface-induced effects in GaN nanowires*, J. Mater. Res. **26** (2011), 2157–2168, DOI: 10.1557/jmr.2011.211.

[56] R. Calarco, M. Marso, T. Richter, A. I. Aykanat, R. Meijers, A. v.d. Hart, T. Stoica, and H. Lüth, *Size-dependent Photoconductivity in MBE-Grown GaN-Nanowires*, Nano Lett. **5** (2005), 981–984, DOI: 10.1021/nl0500306.

[57] H.-Y. Chen, R.-S. Chen, F.-C. Chang, L.-C. Chen, K.-H. Chen, and Y.-J. Yang, *Size-dependent photoconductivity and dark conductivity of m-axial GaN nanowires with small critical diameter*, Appl. Phys. Lett. **95** (2009), 143123, DOI: 10.1063/1.3213556.

[58] J. Wallys, S. Hoffmann, F. Furtmayr, J. Teubert, and M. Eickhoff, *Electrochemical properties of GaN nanowire electrodes–influence of doping and control by external bias*, Nanotechnology **23** (2012), 165701, DOI: 10.1088/0957-4484/23/16/165701.

[59] T. Schumann, T. Gotschke, F. Limbach, T. Stoica, and R. Calarco, *Selective-area catalyst-free MBE growth of GaN nanowires using a patterned oxide layer*, Nanotechnology **22** (2011), 095603, DOI: 10.1088/0957-4484/22/9/095603.

[60] L. Dobos, B. Pécz, L. Tóth, Z. Horváth, Z. Horváth, A. Tóth, E. Horváth, B. Beaumont, and Z. Bougrioua, *Metal contacts to n-GaN*, Appl. Surf. Sci. **253** (2006), 655–661, DOI: 10.1016/j.apsusc.2005.12.167.

[61] G. L. Pearson and J. Bardeen, *Electrical Properties of Pure Silicon and Silicon Alloys Containing Boron and Phosphorus*, Phys. Rev. **75** (1949), 865–883, DOI: 10.1103/PhysRev.75.865.

[62] A. Wolos, Z. Wilamowski, M. Piersa, W. Strupinski, B. Lucznik, I. Grzegory, and S. Porowski, *Properties of metal-insulator transition and electron spin relaxation in GaN:Si*, Phys. Rev. B **83** (2011), 165206, DOI: 10.1103/PhysRevB.83.165206.

[63] F. Furtmayr, *Nitride Nanowire Heterostructures*, Doktorarbeit, Walter Schottky Institut, Technische Universität München (2013).

[64] S. Fritze, A. Dadgar, H. Witte, M. Bügler, A. Rohrbeck, J. Bläsing, A. Hoffmann, and A. Krost, *High Si and Ge n-type doping of GaN doping - Limits and impact on stress*, Appl. Phys. Lett. **100** (2012), 122104, DOI: 10.1063/1.3695172.

[65] G. D. Mahan, *Energy gap in Si and Ge: Impurity dependence*, J. Appl. Phys. **51** (1980), 2634–2646, DOI: 10.1063/1.327994.

[66] D. C. Look, D. C. Reynolds, J. W. Hemsky, J. R. Sizelove, R. L. Jones, and R. J. Molnar, *Defect Donor and Acceptor in GaN*, Phys. Rev. Lett. **79** (1997), 2273–2276, DOI: 10.1103/PhysRevLett.79.2273.

[67] N. Lu and I. Ferguson, *III-nitrides for energy production: photovoltaic and thermoelectric applications*, Semicond. Sci. Technol. **28** (2013), 074023, DOI: 10.1088/0268-1242/28/7/074023.

[68] M. Feneberg, K. Lange, C. Lidig, M. Wieneke, H. Witte, J. Bläsing, A. Dadgar, A. Krost, and R. Goldhahn, *Anisotropy of effective electron masses in highly doped nonpolar GaN*, Appl. Phys. Lett. **103** (2013), 232104, DOI: 10.1063/1.4840055.

[69] M. Feneberg, S. Osterburg, K. Lange, C. Lidig, B. Garke, R. Goldhahn, E. Richter, C. Netzel, M. D. Neumann, N. Esser, S. Fritze, H. Witte, J. Bläsing, A. Dadgar, and A. Krost, *Band gap renormalization and Burstein-Moss effect in silicon- and germanium-doped wurtzite GaN up to* $10^{20}\mathrm{cm}^{-3}$, Phys. Rev. B **90** (2014), 075203, DOI: 10.1103/PhysRevB.90.075203.

[70] D. L. Rode and D. K. Gaskill, *Electron Hall mobility of n-GaN*, Appl. Phys. Lett. **66** (1995), 1972–1973, DOI: 10.1063/1.113294.

[71] E. Cimpoiasu, E. Stern, G. Cheng, R. Munden, A. Sanders, and M. A. Reed, *Electron mobility study of hot-wall CVD GaN and InN nanowires*, Braz. J. Phys. **36** (2006), 824–827, DOI: 10.1590/S0103-97332006000600007.

[72] E. Cimpoiasu, E. Stern, R. Klie, R. A. Munden, G. Cheng, and M. A. Reed, *The effect of Mg doping on GaN nanowires*, Nanotechnology **17** (2006), 5735, DOI: 10.1088/0957-4484/17/23/004.

[73] V. W. L. Chin, T. L. Tansley, and T. Osotchan, *Electron mobilities in gallium, indium, and aluminum nitrides*, J. Appl. Phys. **75** (1994), 7365–7372, DOI: 10.1063/1.356650.

[74] J. Xie, S. Mita, L. Hussey, A. Rice, J. Tweedie, J. LeBeau, R. Collazo, and Z. Sitar, *On the strain in n-type GaN*, Appl. Phys. Lett. **99** (2011), 141916, DOI: 10.1063/1.3647772.

[75] F. Furtmayr, M. Vielemeyer, M. Stutzmann, A. Laufer, B. K. Meyer, and M. Eickhoff, *Optical properties of Si- and Mg-doped gallium nitride nanowires grown by plasma-assisted molecular beam epitaxy*, J. Appl. Phys. **104** (2008), 074309, DOI: 10.1063/1.2980341.

[76] L. I. Aparshina, S. V. Dubonos, S. V. Maksimov, A. A. Svintsov, and S. I. Zaitsev, *Energy dependence of proximity parameters investigated by fitting before measurement tests*, J. Vac. Sci. Technol. B **15** (1997), 2298–2302, DOI: 10.1116/1.589633.

[77] M. Hatzakis, *Electron Resists for Microcircuit and Mask Production*, J. Electrochem. Soc. **116** (1969), 1033–1037, DOI: 10.1149/1.2412145.

Danksagung

An dieser Stelle möchte ich mich recht herzlich bei allen bedanken, die mich während der Zeit als Doktorand am I. Physikalischen Institut der Justus-Liebig-Universität Gießen unterstützt und begleitet haben.

Ich danke...

- Prof. Dr. Martin Eickhoff ganz herzlich dafür, dass ich in seiner Arbeitsgruppe „Nanotechnologische Materialien“ forschen konnte. Sein hoher Anspruch, sowie die intensive Betreuung, viele Ratschläge, Motivationsspritzen und Erklärungen haben zu einer sehr guten Ausbildung geführt. Besonders hat mich immer bestärkt, dass die Technologieentwicklung als große Leistung anerkannt wurde.
- Prof. Dr. Detlev M. Hofmann für viele gute Ideen im Verlauf der letzten Jahre. Immer wieder konnte er mit anschaulichen Erklärungen Fachwissen vermitteln.
- Prof. Dr. Peter J. Klar und Dr. Torsten Henning für die Bereitstellung des MiNa-Labors, sowie Hilfestellung beim Einstieg in die Welt der Nanostrukturierung.
- Dr. Jörg Teubert und Dr. Jörg Schörmann für ihr Fachwissen, das immer wieder geholfen hat, Sachverhalte zu verstehen. Ihr technischer Rat bei praktischen Arbeiten war von nicht geringerem Wert. Herzlichen Dank auch für gute Gesellschaft auf Dienstreisen!
- Pascal Hille, Christian Länger und Marius Günther, die ich während ihren Bachelor- und/oder Masterarbeiten betreuen durfte, für die gute Zusammenarbeit und ihre fleißige Unterstützung bei der Technologieentwicklung und Messungen. Pascal danke ich außerdem für das Wachstum der untersuchten Nanodrähte.
- Jan Müßener für seine Unterstützung bei PL-Messungen und viele konstruktive Diskussionen, sowie sein Interesse an der EBL.
- Dr. Matthias Elm und Patrik Uredat für die Messungen der temperaturabhängigen Leitfähigkeit und ihr Interesse an den empfindlichen Nanodrähten.

- Dr. Martin Feneberg sehr herzlich für die Modellierung der PL-Spektren.
- Max Kracht für seine Hilfe bei der Untersuchung der Proben mittels Rasterkraftmikroskopie.
- Gesche M. Müntze für die gesellige Zeit im gemeinsamen Büro, sowie viele fachliche Diskussionen. Herzlichen Dank auch für die angenehme Gesellschaft auf vielen Dienstreisen.
- Dr. Jens Wallys und Sascha Hoffmann für die aufregende gemeinsame Zeit als erste Doktoranden in der AG Nanotechnologische Materialien.
- Pascal Becker für viele gute praktische Ratschläge, sowie angenehme Gesellschaft auf Dienstreisen.
- allen anderen Mitgliedern der AG Nanotechnologische Materialien von Prof. Dr. Eickhoff, die ich nicht namentlich aufführe, für die schöne Zeit zusammen, sowohl beim Forschen, als auch bei gemeinsamen Aktionen und Verköstigungen.
- auch allen Mitgliedern des I. Physikalischen Instituts für die kollegiale Zusammenarbeit, die ich sehr geschätzt habe.
- meiner Frau für ihre stete Unterstützung während meiner Zeit als Doktorand.

Versicherung

Ich erkläre:
Ich habe die vorgelegte Dissertation selbständig und ohne unerlaubte fremde Hilfe und nur mit den Hilfen angefertigt, die ich in der Dissertation angegeben habe.
Alle Textstellen, die wörtlich oder sinngemäß aus veröffentlichten Schriften entnommen sind, und alle Angaben, die auf mündlichen Auskünften beruhen, sind als solche kenntlich gemacht.
Bei den von mir durchgeführten und in der Dissertation erwähnten Untersuchungen habe ich die Grundsätze guter wissenschaftlicher Praxis, wie sie in der „Satzung der Justus-Liebig-Universität Gießen zur Sicherung guter wissenschaftlicher Praxis“ niedergelegt sind, eingehalten.

Gießen, im November 2014 Markus Georg Schäfer